The Astrophysical Journal, 934:104 (20pp), 2022 August 1 https://doi.org/10.3847/1538-4357/ac7a41

The X-Ray and Radio Loud Fast Blue Optical Transient AT2020mrf: Implications for an Emerging Class of Engine-driven Massive Star Explosions

Yuhan Yao[1], Anna Y. Q. Ho[2,3], Pavel Medvedev[4], Nayana A. J.[5], Daniel A. Perley[6], S. R. Kulkarni[1], Poonam Chandra[7], Sergey Sazonov[4,8], Marat Gilfanov[4,9], Georgii Khorunzhev[4], David K. Khatami[2], and Rashid Sunyaev[4,9]
[1] Division of Physics, Mathematics and Astronomy, California Institute of Technology, Pasadena, CA 91125, USA; yyao@astro.caltech.edu
[2] Department of Astronomy, University of California, Berkeley, 501 Campbell Hall, Berkeley, CA, 94720, USA
[3] Miller Institute for Basic Research in Science, 468 Donner Lab, Berkeley, CA 94720, USA
[4] Space Research Institute, Russian Academy of Sciences, Profsoyuznaya ul. 84/32, Moscow, 117997, Russia
[5] Indian Institute of Astrophysics, II Block, Koramangala, Bangalore 560034, India
[6] Astrophysics Research Institute, Liverpool John Moores University, IC2, Liverpool Science Park, 146 Brownlow Hill, Liverpool L3 5RF, UK
[7] National Centre for Radio Astrophysics, Tata Institute of Fundamental Research, P.O. Box 3, Pune, 411007, India
[8] Moscow Institute of Physics and Technology, Institutsky per. 9, 141700 Dolgoprudny, Russia
[9] Max-Planck-Institut für Astrophysik, Karl-Schwarzschild-Str. 1, D-85741 Garching, Germany
Received 2021 December 1; revised 2022 June 6; accepted 2022 June 17; published 2022 July 28

Abstract

We present AT2020mrf (SRGe J154754.2+443907), an extra-galactic ($z = 0.1353$) fast blue optical transient (FBOT) with a rise time of $t_{g,\rm rise} = 3.7$ days and a peak luminosity of $M_{g,\rm peak} = -20.0$. Its optical spectrum around peak shows a broad ($v \sim 0.1c$) emission feature on a blue continuum ($T \sim 2 \times 10^4$ K), which bears a striking resemblance to AT2018cow. Its bright radio emission ($\nu L_\nu = 1.2 \times 10^{39}$ erg s^{-1}; $\nu_{\rm rest} = 7.4$ GHz; 261 days) is similar to four other AT2018cow-like events, and can be explained by synchrotron radiation from the interaction between a sub-relativistic ($\gtrsim$0.07–0.08c) forward shock and a dense environment ($\dot{M} \lesssim 10^{-3}\, M_\odot$ yr^{-1} for $v_{\rm w} = 10^3$ km s^{-1}). AT2020mrf occurs in a galaxy with $M_* \sim 10^8\, M_\odot$ and specific star formation rate $\sim 10^{-10}$ yr^{-1}, supporting the idea that AT2018cow-like events are preferentially hosted by dwarf galaxies. The X-ray luminosity of AT2020mrf is the highest among FBOTs. At 35–37 days, SRG/eROSITA detected luminous ($L_{\rm X} \sim 2 \times 10^{43}$ erg s^{-1}; 0.3–10 keV) X-ray emission. The X-ray spectral shape ($f_\nu \propto \nu^{-0.8}$) and erratic intraday variability are reminiscent of AT2018cow, but the luminosity is a factor of $\sim$20 greater than AT2018cow. At 328 days, Chandra detected it at $L_{\rm X} \sim 10^{42}$ erg s^{-1}, which is >200 times more luminous than AT2018cow and CSS161010. At the same time, the X-ray emission remains variable on the timescale of $\sim$1 day. We show that a central engine, probably a millisecond magnetar or an accreting black hole, is required to power the explosion. We predict the rates at which events like AT2018cow and AT2020mrf will be detected by SRG and Einstein Probe.

Unified Astronomy Thesaurus concepts: X-ray transient sources (1852); Radio transient sources (2008); Supernovae (1668); Core-collapse supernovae (304); High energy astrophysics (739); Sky surveys (1464)

1. Introduction

The past few years have shown that the landscape of massive-star death is unexpectedly rich and diverse. Of particular interest is the group of "fast blue optical transients" (FBOTs; Drout et al. 2014; Pursiainen et al. 2018). As implied by the name, these events exhibit blue colors of $(g - r) < -0.2$ mag at peak and evolve faster than ordinary supernovae (SNe), with time above half-maximum $t_{1/2} \lesssim 12$ days.

The earliest studies were stymied by the identification of FBOTs after the transients had faded away. This situation has been rectified by cadenced wide-field optical sky surveys, such as the Zwicky Transient Facility (ZTF; Bellm et al. 2019; Graham et al. 2019) and the Asteroid Terrestrial-impact Last Alert System (ATLAS; Tonry et al. 2018), which enable real-time discovery and spectroscopic classification. Ho et al. (2021a) recently identified three distinct subtypes of FBOTs: (1) subluminous stripped-envelope SNe of type Ib/IIb, (2) luminous interaction-powered SNe of type IIn/Ibn/Icn, and (3) the most luminous ($-20 \lesssim M_{\rm peak} \lesssim -22$) and short-duration ($t_{1/2} \lesssim 5$ days) events with properties similar to AT2018cow.

The nature of AT2018cow-like events remains mysterious. Following the discovery of the prototype AT2018cow ($z = 0.014$, Prentice et al. 2018), only three analogs have been identified: AT2018lug ($z = 0.271$, Ho et al. 2020), CSS161010 ($z = 0.034$; Coppejans et al. 2020), and AT2020xnd ($z = 0.243$, Perley et al. 2021). All of these events arose in low-mass star-forming galaxies, which suggests a massive star origin and disfavors models invoking tidal disruption by an intermediate-mass black hole (Perley et al. 2021). In the radio and millimeter band, their high luminosities imply the existence of dense circumstellar material (CSM), which points to significant mass loss prior to the explosion (Ho et al. 2019; Huang et al. 2019; Margutti et al. 2019; Coppejans et al. 2020).

The X-ray luminosity of AT2018cow ($\sim 10^{43}$ erg s^{-1}) at early times ($\lesssim$20 days) is similar to that of long-duration gamma-ray bursts (GRBs; Rivera Sandoval et al. 2018). Its fast soft X-ray variability suggests the existence of a central energy source (also called central engine), and the relativistic reflection features seen in the hard X-ray spectrum point to equatorial materials (Margutti et al. 2019). The probable natures of the central engine include an accreting black hole, a rapidly spinning magnetar, and an embedded internal shock (Margutti et al. 2019; Pasham et al. 2022). Meanwhile, AT2018cow's late-time (~20–45 days) optical spectra are dominated by hydrogen and helium (Perley et al. 2019; Margutti et al. 2019;

Xiang et al. 2021), which make it different from other engine-powered massive stellar transients such as long GRBs and hydrogen-poor super-luminous supernovae (i.e., SLSNe-I; see a recent review by Gal-Yam 2019) that are devoid of hydrogen and helium.

X-ray observations of AT2020xnd showed a luminosity consistent with that of AT2018cow at 20–40 days (Bright et al. 2022; Ho et al. 2021b). Separately, late-time ($\gtrsim$100 day) observations of AT2018cow and CSS161010 showed modest X-ray emission at $L_{\rm X} \approx$ few $\times\ 10^{39}$ erg s^{-1}) (see Appendix A and Coppejans et al. 2020). AT2018cow-like events are thus promising X-ray transients to be discovered by the eROSITA (Predehl et al. 2021) and the Mikhail Pavlinsky ART-XC (Pavlinsky et al. 2021) telescopes onboard the Spektrum–Roentgen–Gamma (SRG) satellite (Sunyaev et al. 2021).

AT2020mrf is an FBOT that was first detected by ZTF on 2020 June 12. On June 14, it was also detected by ATLAS. On July 15, it was reported to the transient name server (TNS) by the ATLAS team (Tonry et al. 2020). On June 17, an optical spectrum obtained by the "Global SN Project" displayed a featureless blue continuum. Burke et al. (2020) assigned a spectral type of "SN II" and tentatively associated it with a $z = 0.059$ host galaxy (109″ offset). AT2020mrf was detected in the X-ray by SRG from 2020 July 21 to July 24 (Section 2.3), which made it a promising candidate AT2018cow analog and motivated our follow-up observations. Given that the SRG detection occurred ∼41 days after the first optical detection, and we became aware of it even later, our follow-up started in April 2021.

This paper is organized as follows. We outline optical, X-ray, and radio observations, as well as analysis of AT2020mrf and its host galaxy ($z = 0.1353$) in Section 2. We provide the forward shock and CSM properties in Section 3.1, discuss possible power sources of the optical emission in Section 3.2, and present host galaxy properties in Section 3.3. We summarize AT2020mrf's key X-ray properties and discuss the implication in the context of engine-driven explosions similar to AT2018cow in Section 3.4. We estimate the detection rates of events like AT2018cow and AT2020mrf in current and upcoming X-ray all-sky surveys in Section 4. Finally, we give a summary in Section 5.

UT time is used throughout the paper. We assume a cosmology of $\Omega_{\rm M} = 0.3$, $\Omega_\Lambda = 0.7$, and $h = 0.7$, implying a luminosity distance to AT2020mrf of $D_L = 637$ Mpc and an angular-diameter distance of $D_\theta = 494$ Mpc. Optical magnitudes are reported in the AB system. We use the Galactic extinction from Schlafly & Finkbeiner (2011) and the extinction law from Cardelli et al. (1989). Coordinates are given in J2000.

2. Observations and Data Analysis

2.1. Optical Photometry

We obtained public ZTF[10] and ATLAS[11] forced photometry (Masci et al. 2019; Smith et al. 2020) using the median position of all ZTF alerts (R. A. = $15^{\rm h}47^{\rm m}54\overset{\rm s}{.}17$, decl. = $+44°39'07\overset{''}{.}34$). The 1-day binned optical light curve is shown in Figure 1. Following Whitesides et al. (2017) and Ho et al. (2020), we compute absolute magnitude using

$$M = m_{\rm obs} - 5\log_{10}\left(\frac{D_L}{10\ {\rm pc}}\right) + 2.5\log_{10}(1+z) \qquad (1)$$

The last term in Equation (1) is a rough estimation of the K-correction, and introduces an error of 0.1 mag.

The first detection is $r = 20.88 \pm 0.17$, on 2020-06-12T06:14:12 (59012.2599 MJD) and the last non-detection is $o > 21.73$, on 2020-06-11T10:12:13 (59011.4252 MJD). Therefore, we assume an explosion epoch of $t_0 = 59012.0$ MJD. Hereafter, we use Δt to denote rest-frame time with respect to t_0. At $\Delta t = 3.7$ days, AT2020mrf peaked at $M_g = -20.0$ mag.

2.2. Optical Spectroscopy

The transient spectrum[12] was obtained on 2020 June 17 ($\Delta t = 4.8$ days) with the FLOYDS-N spectrograph on the 2 m Faulkes Telescope North (Burke et al. 2020). As shown in Figure 2, the spectrum is similar to that of AT2018cow at similar phases—a single broad feature at ∼5600 Å was observed to span ±600 Å, indicating a velocity of 0.1c. The origin of this broad line in AT2018cow remains an open question. Perley et al. (2019) note that although it is vaguely reminiscent of the Fe II feature in Ic broad-line (Ic-BL) SNe around peak (Galama et al. 1998), in SNe Ic-BL the blueshifted absorption trough strengthens at later times, while in AT2018cow this line vanished at $\Delta t \sim 8$ days. In terms of other AT2018cow-like objects, the peak-light optical spectra of AT2018lug and AT2020xnd are consistent with being blue and featureless (Ho et al. 2020; Perley et al. 2021), and there exists no published optical spectra of CSS161010.

A blackbody fit to AT2020mrf's optical spectrum suggests a temperature of $T \approx 2 \times 10^4$ K and a radius of $R = 7.9 \times 10^{14}$ cm. This temperature is typical of AT2018cow-like events.

2.3. Early-time X-Rays: SRG

SRG is a space satellite at the L2 Lagrange point with a drafting rate of $\approx 1°$ day^{-1}. It is conducting eight all-sky surveys from the beginning of 2020 to the end of 2023, with a cadence of 6 months. Hereafter, eRASSn refers to the n'th eROSITA all-sky survey. SRG's rotational axis points toward the Sun, and the rotational period is 4 hr. The eROSITA field-of-view (FoV) is 1 deg^2. Therefore, during a single sky survey, a particular region of the sky will be scanned by eROSITA at least ∼6 times (∼1 day), where each scan lasts for ≈40 s (see details in Sunyaev et al. 2021). AT2020mrf, at a relatively high ecliptic latitude of $b_{\rm ecl} = 61\overset{\circ}{.}9$, was scanned for ≈3 days in each all-sky survey.

During eRASS2 ($\Delta t \sim 36$ days), SRG/eROSITA discovered an X-ray transient SRGe J154754.2 + 443907, with a 98% localization radius of $4\overset{''}{.}28$. SRGe J154754.2 + 443907 is only $0\overset{''}{.}56$ from AT2020mrf (see Figure 3), suggesting an association between the X-ray and the optical transients. Figure 4 shows that the source exhibits significant variability—the 0.2–2.2 keV count rate increased from ≈ 0.053 count s^{-1} ($\Delta t \sim 35$ days) to ≈ 0.32 count s^{-1} ($\Delta t \sim 36$ days), and then decreased to ≈ 0.051 count s^{-1} ($\Delta t \sim 37$ days).

Figure 5 shows the average eRASS2 spectrum of AT2020mrf, which has been grouped via `ftgrouppha` to have at least five

[10] https://ztfweb.ipac.caltech.edu/cgi-bin/requestForcedPhotometry.cgi
[11] https://fallingstar-data.com/forcedphot/

[12] Available at https://www.wis-tns.org/object/2020mrf.

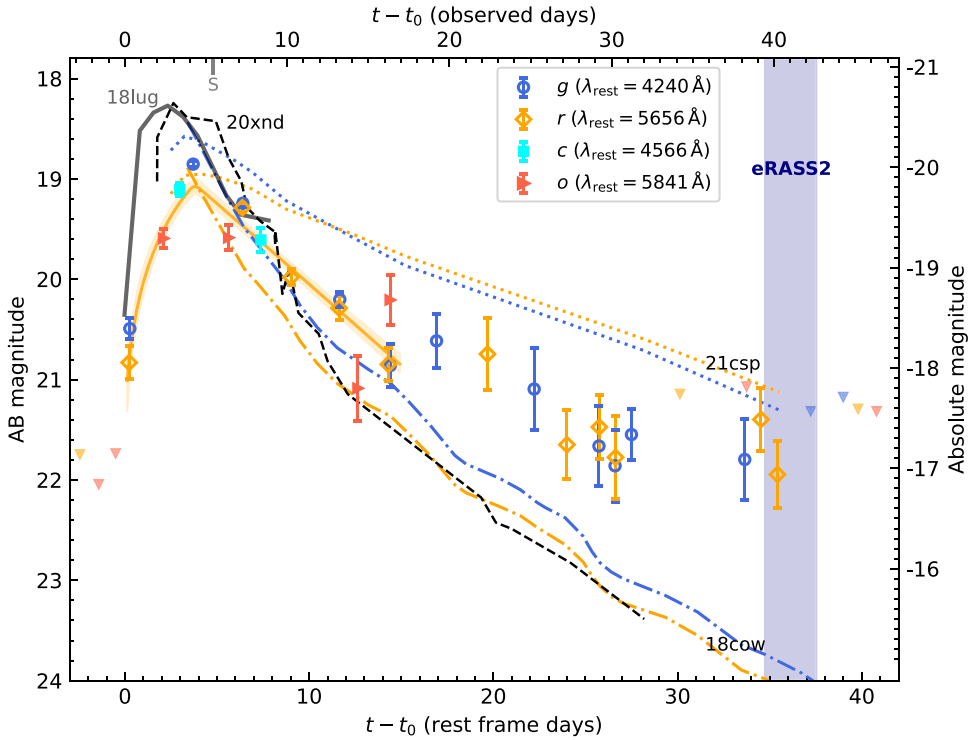

Figure 1. Optical (ZTF *gr*, ATLAS *co*) light curve of AT2020mrf (data points are $>2.5\sigma$ detections, semitransparent downward triangles are 3 σupper limits). The "S" tick along the upper axis marks the epoch of spectroscopy (Section 2.2). The solid orange line is a simple r_{ZTF}-band model fitted to data round maximum (see Section 3.2). The SRG eRASS2 scan duration is marked by the vertical blue band (Section 2.3). The rest-frame equivalent light curves of AT2018cow and AT2021csp are shown as dashed–dotted lines (based on blackbody parameters provided in Table 4 of Perley et al. 2019) and dotted lines (based on Table 4 of Perley et al. 2022), respectively. The solid and dashed black lines are observer-frame r_{ZTF}-band light curves of AT2018lug ($\lambda_{rest} = 5050$ Å) and AT2020xnd ($\lambda_{rest} = 5165$ Å), respectively. Note that the apparent AB magnitude scale pertains to AT2020mrf only—the light curves of other objects are only shown in absolute magnitude.

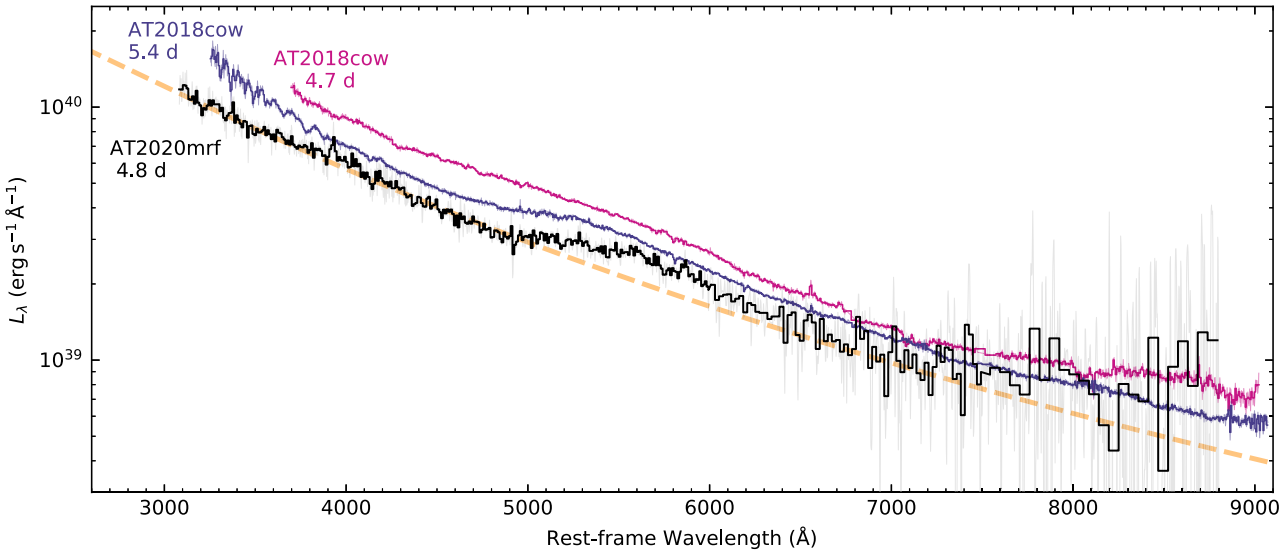

Figure 2. Optical spectrum of AT2020mrf, compared with AT2018cow at similar phases (Perley et al. 2019). The dashed line is a blackbody with $T = 2 \times 10^4$ K and $R = 7.9 \times 10^{14}$ cm.

counts per bin in the background spectrum. We fit the 0.3–10 keV spectrum using `xspec` (12.11, Arnaud 1996) and *C*-statistics. The data are modeled first with an absorbed power-law (`zpowerlw`) and then with an absorbed thermal plasma (`apec`). For each model, we first fix the column density at the Galactic value of $N_H = 1.38 \times 10^{20}$ cm^{-2} (Willingale et al. 2013), and then free this parameter. The models with fixed N_H are shown in Table 1. The data do not favor any particular model because the *cstat*/*dof* (*C*-statistics divided by degrees of freedom) values have small differences between the four fits.

Although we are unable to distinguish between the power-law and thermal models using the eROSITA data, the optical/

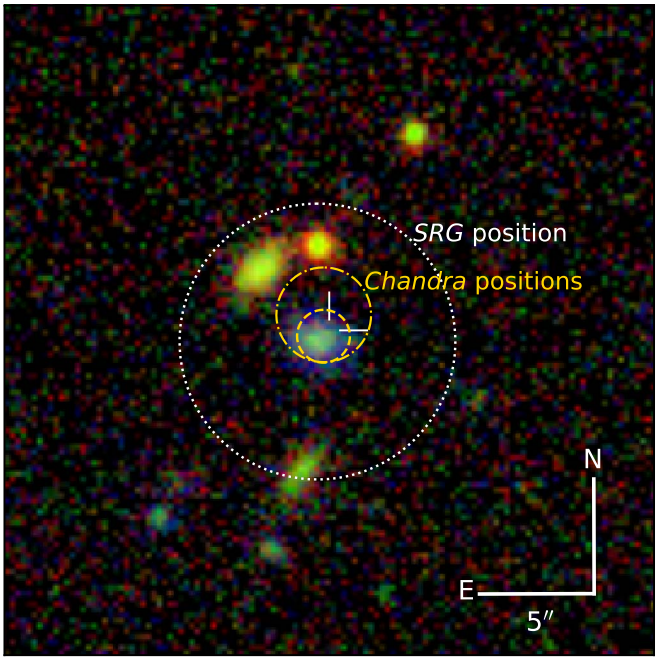

Figure 3. HSC-SSP RGB false-color $g/i/z$ image centered at the ZTF position of AT2020mrf (marked by the white crosshairs). AT2020mrf is an off-nuclear source $0\farcs50$ offset from the host centroid. The position of the X-ray transient detected by SRG/eROSITA is shown with a dotted circle, where the radius represents the $4\farcs28$ uncertainty (98% confidence). The more accurate positions provided by Chandra obsID 25050 and obsID 25064 are shown with a dashed–dotted circle and a dashed circle (1σ confidence), respectively.

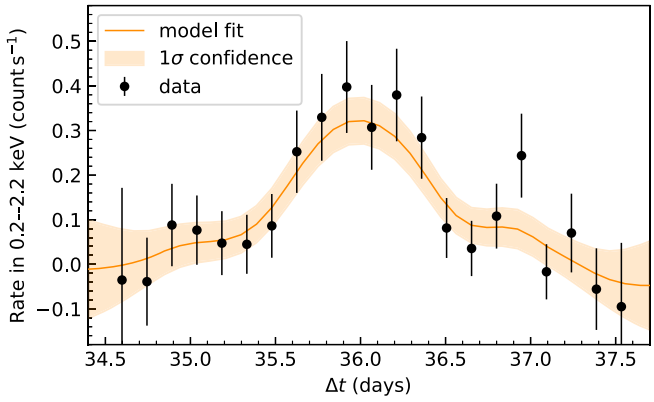

Figure 4. eRASS2 light curve of AT2020mrf. Count rate uncertainties are estimated using Gehrels' approximation (Gehrels 1986). The orange curve is a fit to the data, generated using a Gaussian process model following procedures laid out in Appendix B.4 of Yao et al. (2020).

radio similarities between AT2020mrf and AT2018cow (Sections 2.1, 2.2, 3.1), and the non-thermal nature of AT2018cow's X-rays ($f_\nu \propto \nu^{-0.7}$, 36.5 days, 0.3–30 keV, see Figure 6 of Margutti et al. 2019) motivate us to adopt the power-law model in the following discussion.

AT2020mrf was not detected in eRASS1, eRASS3 and eRASS4. Using the eROSITA sensitivity maps, we calculate the 0.3–2.2 keV flux upper limits to be $(1.12,\ 1.35,\ 1.54) \times 10^{-14}$ erg s^{-1} cm^{-2} at the confidence level likelihood of 6 ($\approx 2.8\sigma$).

2.4. Late-time X-Rays: Chandra

We conducted deep X-ray observations of AT2020mrf with the Chandra X-ray Observatory (Wilkes & Tucker 2019) under

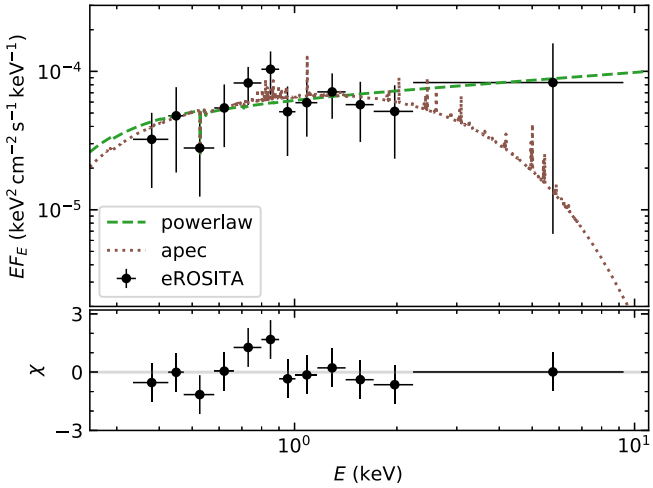

Figure 5. eRASS2 spectrum of AT2020mrf. We show the best-fit power-law model (dashed green line, $f_\nu \propto \nu^{-0.8}$) and thermal plasma model (dotted brown line, $k_{\rm B}T \sim 2.0$ keV) with $N_{\rm H}$ fixed at the Galactic value (see Table 1).

a DDT program (PI Yao) on 2021 June 18 (22.0 ks, obsID 25050) and June 19 (19.8 ks, obsID 25064). We used the Advanced CCD Imaging Spectrometer (ACIS; Garmire et al. 2003), with the aim point on the back illuminated CCD S3. The data were reduced with the `CIAO` package (v4.14).

To determine the astrometric shifts of Chandra images, we first ran the `CIAO` tool `wavdetect` to obtain lists of positions for all sources in the Chandra FoV. Wavelet scales of 1, 2, 4, and 8 pixels and a significance threshold of 10^{-6} were used. A total of 8 and 12 X-ray sources were detected in obsID 25050 and obsID 25064, respectively. We cross matched the X-ray source lists with the Gaia EDR3 catalog (Gaia Collaboration et al. 2021), using a radius of $2''$. This left two Chandra/Gaia sources from both obsIDs. We define the astrometric shifts as the mean difference in R.A. and decl. between the two matched sources. For obsID 25050, δ R.A. $= -1.88 \pm 0\farcs42$ and δ decl. $= -0.58 \pm 0\farcs75$; For obsID 25064, δ R.A. $= -0.62 \pm 0\farcs27$ and δ decl $= +0.61 \pm 0\farcs29$.

Having applied the astrometric shifts, we found that an X-ray source at the location of AT2020mrf was detected in both obsIDs. The position of the X-ray source from obsID 25050 is R. A. $= 15^{\rm h}47^{\rm m}54\fs18$, decl. $= +44°39'07\farcs83$, with an astrometric uncertainty of $1\farcs47$ from the residual offsets with the Gaia catalog. The position of the X-ray source from obsID 25064 is R. A. $= 15^{\rm h}47^{\rm m}54\fs18$, decl.$=+44°39'07\farcs16$, with an astrometric uncertainty of $0\farcs82$ from the residual offsets with the Gaia catalog. The Chandra positions are shown in Figure 3, which are more accurate than the eROSITA position, and clearly associate the X-ray emission with the ZTF position of AT2020mrf.

For each obsID, we extracted the source spectrum using a source region of $r_{\rm src} = 1\farcs5$ centered on the X-ray position determined by `wavdetect`. A total of 30 and 10 counts (0.5–10 keV) were detected within the source regions of obsID 25050 and obsID 25064, respectively. The background spectrum was extracted using nearby source-free regions. The 0.5–10 keV net count rate at 90% credible interval is $1.61^{+0.32}_{-0.28} \times 10^{-3}$ count s^{-1} for obsID 25050, and $0.56^{+0.21}_{-0.17} \times 10^{-3}$ count s^{-1} for obsID 25064, indicating that X-ray net count rate has dropped by a factor of 2.9 ± 1.1. Such a large flux decrease reflects intrinsic X-ray variability.

Table 1
Modeling of the eRASS2 Spectrum

Component	Parameter	Power-law Model		Thermal Plasma Model	
		(a) Fixed $N_{\rm H}$	(b) Free $N_{\rm H}$	(a) Fixed $N_{\rm H}$	(b) Free $N_{\rm H}$
tbabs	$N_{\rm H}$ (10^{20} cm^{-2})	1.38	$15.32^{+14.06}_{-10.70}$	1.38	$9.04^{+7.10}_{-6.99}$
zpowerlw	Γ	1.81 ± 0.26	$2.79^{+1.00}_{-0.80}$	...	...
	norm$_{\rm pl}$ (10^{-5})	$8.0^{+1.1}_{-1.0}$	$14.8^{+11.8}_{-5.7}$	...	...
apec	$k_{\rm B}T$	...	...	$2.0^{+1.9}_{-0.7}$	$1.0^{+1.1}_{-0.3}$
	norm$_{\rm apec}$ (10^{-4})	...	...	$3.8^{+0.9}_{-0.7}$	$7.2^{+5.2}_{-3.3}$
cstat/*dof*		25.94/35	24.09/34	24.80/35	23.60/34
Observed 0.3–10 keV flux (10^{-13} erg s^{-1} cm^{-2})		$3.90^{+1.32}_{-1.00}$	$2.48^{+0.51}_{-0.83}$	$2.40^{+0.54}_{-0.75}$	$1.92^{+0.15}_{-1.37}$

Note. Norm$_{\rm pl}$ and norm$_{\rm apec}$ are the normalization parameters in the model components (see the xspec documentation for units). Uncertainties are represented by the 68% confidence intervals.

We grouped the Chandra spectrum to at least one count per bin, and modeled the data using *C*-statistics. We used a model of tbabs*zpowerlw, with $N_{\rm H}$ fixed at the Galactic value. Since the count rate has significantly decreased between the two obsIDs, we include a constant scaling factor $\mathcal{C}$ between the two Chandra observations (Madsen et al. 2017), with the constant for obsID 25050 ($\mathcal{C}_1$) fixed at 1. The result, with *cstat*/*dof* = 32.25/34, gives $\Gamma = 1.00 \pm 0.35$ and $\mathcal{C}_2 = 0.39^{+0.17}_{-0.13}$, where uncertainties are represented by the 68% confidence intervals. The best-fit model is shown in Figure 6.

The difference between the SRG and Chandra power-law indices is $\Gamma_{36\,\rm d} - \Gamma_{328\,\rm d} = 0.81 \pm 0.44$. Therefore, we conclude that a change of Γ is marginally detected at 1.9σ. Table 2 summarizes the 0.3–10 keV fluxes.

Figure 7 compares the X-ray luminosity evolution of AT2020mrf with other types of explosions. We further discuss this figure in Section 3.4.

2.5. Search for Prompt γ-Rays

Given that cosmological long GRBs are the only type of massive-star explosion with X-ray luminosities known to be comparable to AT2020mrf (see Figure 7), we are motivated to search for bursts of prompt γ-rays between the last ZTF non-detection and the first ZTF detection (Section 2.1). During this time interval, only one burst was detected by the interplanetary network (IPN; Hurley et al. 2010). The position of this burst (Sonbas et al. 2020) is inconsistent with that of AT2020mrf. To obtain a constraint on the γ-ray flux of AT2020mrf, we use the Konus instrument (Aptekar et al. 1995) on the Wind spacecraft. Unlike other high energy telescopes on low Earth orbit (LEO) spacecraft (such as Swift/BAT and Fermi/GBM), Konus-Wind (KW) continuously observes the whole sky without Earth blocking and with a very stable background thanks to its orbit around the L1 Lagrange point (see, e.g., Tsvetkova et al. 2021). During the interval of interest, KW was taking data (total duration of data gaps was $< 1\%$ of the total time). Assuming a typical long GRB spectrum[13] and a timescale of 2.944 s, KW gives a 20–1000 keV upper limit of $< 2 \times 10^{-7}$ erg s^{-1} cm^{-2}. This corresponds to an isotropic luminosity of $L_{\rm iso} < 1.0 \times 10^{49}$ erg s^{-1}, which strongly disfavors an on-axis classical GRB (Frail et al. 2001).

[13] The Band function with peak energy $E_{\rm peak} = 300$ keV, low-energy photon index $\alpha = -1$, and high energy photon index $\beta = -2$ (Band et al. 1993).

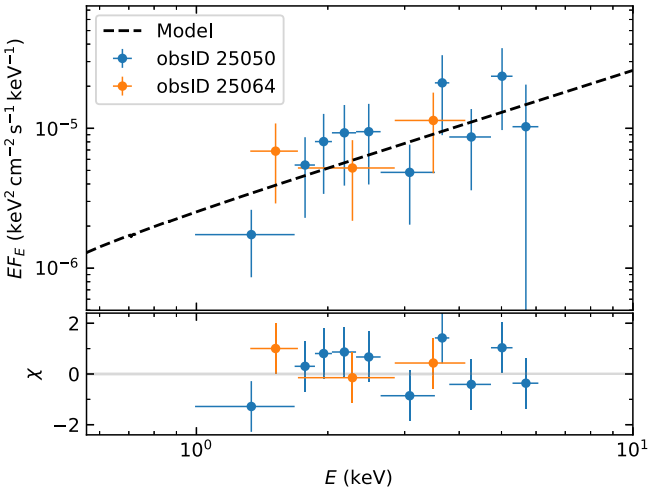

Figure 6. Chandra spectrum of AT2020mrf at $\Delta t \approx 328$ days. The data have been rebinned for visual clarity. The dashed line is the best-fit model ($f_\nu \propto \nu^{+0.0}$). To account for the flux variation (see text), the obsID 25064 data has been divided by 0.39.

Table 2
X-Ray Flux Measurements of AT2020mrf

Δt (days)	Telescope	Observed 0.3–10 keV flux (10^{-14} erg s^{-1} cm^{-2})
−127	SRG/eRASS1	<2.93
34.5–37.6	SRG/eRASS2	$39.0^{+13.2}_{-10.0}$
192	SRG/eRASS3	<7.24
327.4	Chandra	$4.00^{+0.68}_{-1.24}$
328.2		$1.57^{+0.27}_{-0.49}$
355	SRG/eRASS4	<8.26

Note. To convert the 0.3–2.2 keV eROSITA upper limits to 0.3–10 keV, we assume the eRASS2 best-fit spectral model for the eRASS1 epoch, and the Chandra spectral model for the eRASS3 and eRASS4 epochs.

2.6. Radio: VLA and uGMRT

We began a monitoring program of AT2020mrf using the VLA (Perley et al. 2011) under Program 21A-308 (PI Ho), and the upgraded Giant Metrewave Radio Telescope (uGMRT; Swarup 1991; Gupta et al. 2017) under Program 40_077 (PI Nayana). The data were analyzed following the standard radio

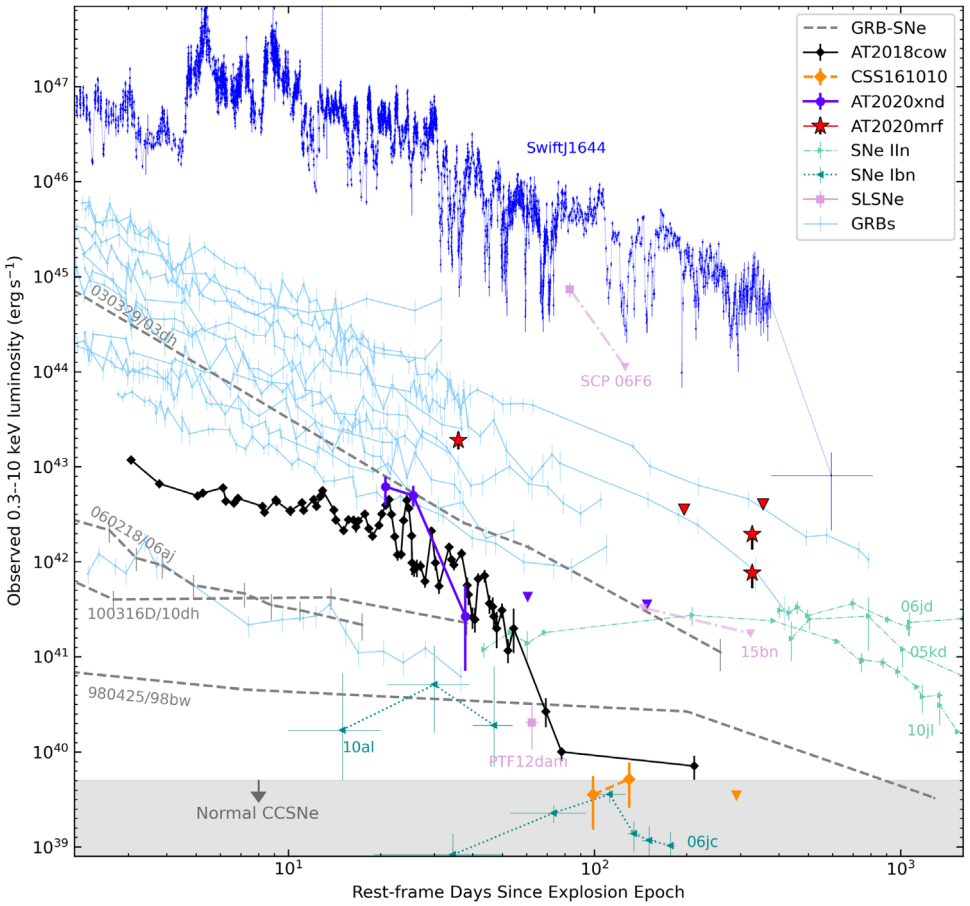

Figure 7. X-ray emission of AT2020mrf, compared with AT2018cow (Rivera Sandoval et al. 2018; Margutti et al. 2019, Appendix A), CSS161010 (Coppejans et al. 2020), AT2020xnd (Bright et al. 2022; Ho et al. 2021b), cosmological long GRBs (light blue solid lines; Appendix B), GRBs associated with SNe (dashed gray lines; Kouveliotou et al. 2004; Tiengo et al. 2004; Campana et al. 2006; Soderberg et al. 2006; Margutti et al. 2013), SLSNe-I (Levan et al. 2013; Margutti et al. 2018), the jetted TDE SwiftJ1644 (Mangano et al. 2016), interacting SNe of type IIn (dashed-dotted green lines; Chandra et al. 2012, 2015; Dwarkadas et al. 2016; Katsuda et al. 2016) and type Ibn (dotted cyan lines; Immler et al. 2008; Ofek et al. 2013), as well as normal CCSNe (Dwarkadas & Gruszko 2012). AT2020mrf is as luminous as cosmological GRBs.

continuum image analysis procedures in the Common Astronomy Software Applications (CASA; McMullin et al. 2007). The results are presented in Table 3. Incidentally, AT2020mrf was not detected in the Karl G. Jansky Very Large Array Sky Survey (VLASS, Lacy et al. 2020), which provides a 3σ upper limit of 0.42 mJy at 2–4 GHz in 2019 March. Hereafter, radio flux density values have been K-corrected and frequency values are reported in the rest-frame. K-correction was performed following Condon & Matthews (2018), assuming a steep synchrotron spectrum with a spectral index of $\beta = -1$ ($f_\nu \propto \nu^\beta$).

Regarding data obtained within (Δt /10) days as coeval, we model the radio spectral energy distribution (SED) at $\Delta t \approx 261$ days and $\Delta t \approx 417$ days with a broken power law (Granot & Sari 2002):

$$L_\nu = L_{\nu\ \mathrm{peak}} \left[\left(\frac{\nu}{\nu_{\mathrm{peak}}} \right)^{-s\beta_1} + \left(\frac{\nu}{\nu_{\mathrm{peak}}} \right)^{-s\beta_2} \right]^{-1/s} \quad (2)$$

where ν and L_ν are quantities in the object's rest frame, $L_{\nu\ \mathrm{peak}}$ is the peak specific luminosity, ν_{peak} is the peak frequency, β_1 and β_2 are the asymptotic spectral indices below and above the break, and s is a smoothing parameter. We perform the fit using the Markov chain Monte Carlo (MCMC) approach with emcee (Foreman-Mackey et al. 2013). The reported uncertainties follow from the 68% credible region.

The best-fit models are shown in Figure 8. At $\Delta t \approx 261$ days, $\nu_{\mathrm{peak}} = 7.44^{+0.44}_{-0.52}$ GHz, $L_{\nu\ \mathrm{peak}} = 1.70^{+0.23}_{-0.09} \times 10^{29}$ erg s^{-1} Hz^{-1}, $\beta_1 = 1.3^{+0.4}_{-0.2}$, and $\beta_2 = -1.0 \pm 0.1$. At $\Delta t \approx 305$ days, the 1–4 GHz band probably remains below the broken frequency, and the blue data in Figure 8 suggests $\beta_1 > 1.7$. At $\Delta t \approx 417$ days, $\nu_{\mathrm{peak}} = 4.82^{+1.36}_{-1.18}$ GHz, $L_{\nu\ \mathrm{peak}} = 4.33^{+0.36}_{-0.34} \times 10^{28}$ erg s^{-1} Hz^{-1}, $\beta_1 = 0.4^{+0.3}_{-0.2}$, and $\beta_2 = -0.5 \pm 0.1$. Equation (2) does not provide a decent description for the data.

The radio observations will further be discussed in Section 3.1.

2.7. The Host Galaxy

2.7.1. Observations

Deep pre-explosion images of the target field are available in the Hyper Suprime-Cam Subaru Strategic Program (HSC-SSP; Aihara et al. 2018) second Public Data Release (PDR2; Aihara et al. 2019) and the Galaxy Evolution Explorer (GALEX; Martin et al. 2005) UV imaging survey. As is shown in the left-hand panel of Figure 9, AT2020mrf is $0\farcs50$ offset from an extended blue source (R. A. $= 15^{\mathrm{h}}47^{\mathrm{m}}54\fs20$,

Table 3
Radio Observations of AT2020mrf

Date in 2021	Δt (days)	Telescope/ Receiver	ν_0 (GHz)	f_ν (μJy)
Apr 2	259.5	VLA/C	4.30	254 ± 25
			4.94	234 ± 22
			5.51	330 ± 18
			6.49	327 ± 20
			7.06	336 ± 17
			7.70	349 ± 18
Apr 6	262.9	VLA/S	3.00	165 ± 26
		VLA/X	8.49	277 ± 23
			9.64	271 ± 20
			11.13	223 ± 17
		VLA/Ku	12.78	213 ± 19
			14.32	189 ± 16
			16.62	153 ± 15
		VLA/K	20.00	149 ± 8
			24.00	103 ± 8
May 19	300.9	uGMRT/B5	1.25	<45
May 29	309.5	VLA/S	3.00	206 ± 48
Aug 13	376.6	uGMRT/B5	1.25	<105
Sep 28	416.8	uGRMT/B5	1.36	68 ± 15
Sep 28–29	417.5	VLA/S	3.00	81 ± 10
		VLA/C	6.00	87 ± 7
		VLA/X	10.00	49 ± 8
		VLA/Ku	13.55	65 ± 6
			16.62	51 ± 7

Note. ν_0 is observed central frequency. f_ν is the observed flux density values. Upper limits are 3σ.

decl.=+44°39′07.″01), which is considered to be the host galaxy. At the host redshift, the spatial offset corresponds to a physical distance of 1.19 kpc. The photometry of the host is shown in Table 4.

On 2021 April 14 ($\Delta t = 267.0$ days), we obtained a spectrum of the host galaxy using the Low Resolution Imaging Spectrometer (LRIS; Oke et al. 1995) on the Keck I 10 m telescope. We used the 560 dichroic, the 400/3400 grism on the blue side, the 400/8500 grating on the red side, and the 1″ slit width. This setup gives a full-width half maximum (FWHM) of ≈6.8 Å. Exposure times were 3650 and 3400 s for the blue and red cameras, respectively. The spectrum (upper panel of Figure 9) was reduced and extracted using `LPipe` (Perley 2019).

2.7.2. Analysis

To determine the redshift and emission line fluxes of the host, we fit the Galactic extinction corrected LRIS spectrum with stellar population models using the penalized pixel-fitting (`ppxf`) software (Cappellari & Emsellem 2004; Cappellari 2017). We use the MILES library (FWHM = 2.5 Å; Falcón-Barroso et al. 2011) and commonly observed galaxy emission lines, including Hα, Hβ, Hγ, [O II], [S II], [O III], [O I], and [N II]. The [O I] $\lambda\lambda$ 6300, 6364, [O III] $\lambda\lambda$ 4959, 5007 and [N II] $\lambda\lambda$ 6548, 6583 doublets are fixed at the theoretical flux ratio of 3.

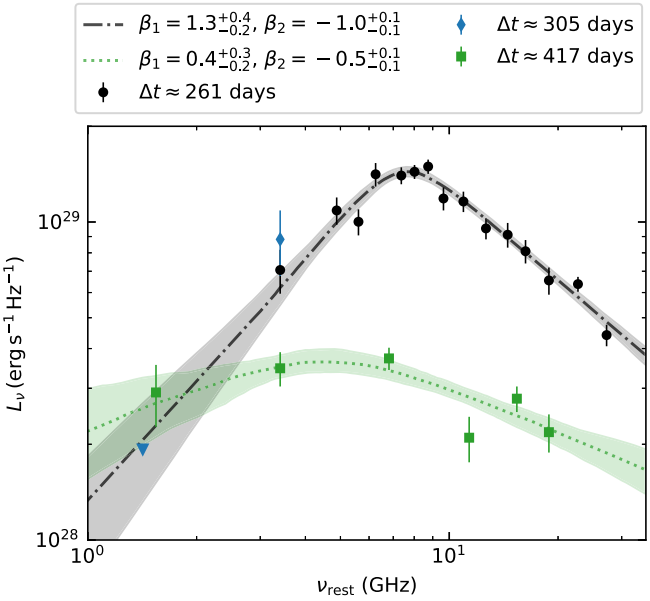

Figure 8. Radio observations of AT2020mrf, overplotted with the best-fit broken power-law models.

The best-fit model suggests a redshift of $z = 0.1353 \pm 0.0002$. Zoom-in portions of the spectrum around regions of emission lines are shown in the bottom panel of Figure 9. The line fluxes are presented in Table 5. Note that because the [O II] doublets are not resolved, the derived individual line fluxes are not reliable and we only report the total flux of the doublets.

The calculated line ratios are given in Table 6. Uncertainties in line ratios are calculated by performing 10^4 Monte Carlo (MC) trials using the measured flux uncertainties. Figure 10 shows the location of the host galaxy on the Baldwin, Phillips, & Terlevich (BPT) diagrams (Baldwin et al. 1981). Under the diagnostic definitions of Kewley et al. (2006), the host falls in the region of star-forming galaxies.

We measure the oxygen abundance using two metallicity indicators N2 and O3N2 (Pettini & Pagel 2004), which are defined in Table 6. Using the calibration reported by Marino et al. (2013), the gas-phase oxygen abundance is $< 8.40 \pm 0.16$(sys) in the N2 scale, and $>8.17 \pm 0.18$(sys) in the O3N2 scale. Compared with the solar metallicity ($Z_\odot$) of $12 + \log(\mathrm{O/H}) = 8.69$ (Asplund et al. 2009), our constraints suggest a metallicity of $10^{-0.70}$–$10^{-0.13} Z_\odot$.

To obtain an estimate of the host galaxy total stellar mass (M_*), we fit the host SED with flexible stellar population synthesis (FSPS; Conroy & Wechsler 2009) models (Foreman-Mackey et al. 2014). We adopt a delayed exponentially declining star formation history (SFH) characterized by the e-folding timescale $\tau_{\rm SFH}$, such that the time-dependent star formation rate $\psi_*(t) \propto te^{-(t/\tau_{\rm SFH})}$. The `Prospector` package (Johnson et al. 2021) was used to run a MCMC sampler (Foreman-Mackey et al. 2013). We use log-uniform priors for the following three parameters: M_* in the range [$10^7 M_\odot$, $10^9 M_\odot$], $\tau_{\rm SFH}$ in the range [0.1 Gyr, 100 Gyr], the metallicity $\log(Z/Z_\odot)$ in the range -0.70 and -0.13, and the population age $t_{\rm age}$ in the range [0.1 Gyr, 12.5 Gyr]. Host galaxy extinction was included, with $E(B-V)_{\rm host}$ uniformly sampled between 0 and 1. From the marginalized posterior probability functions

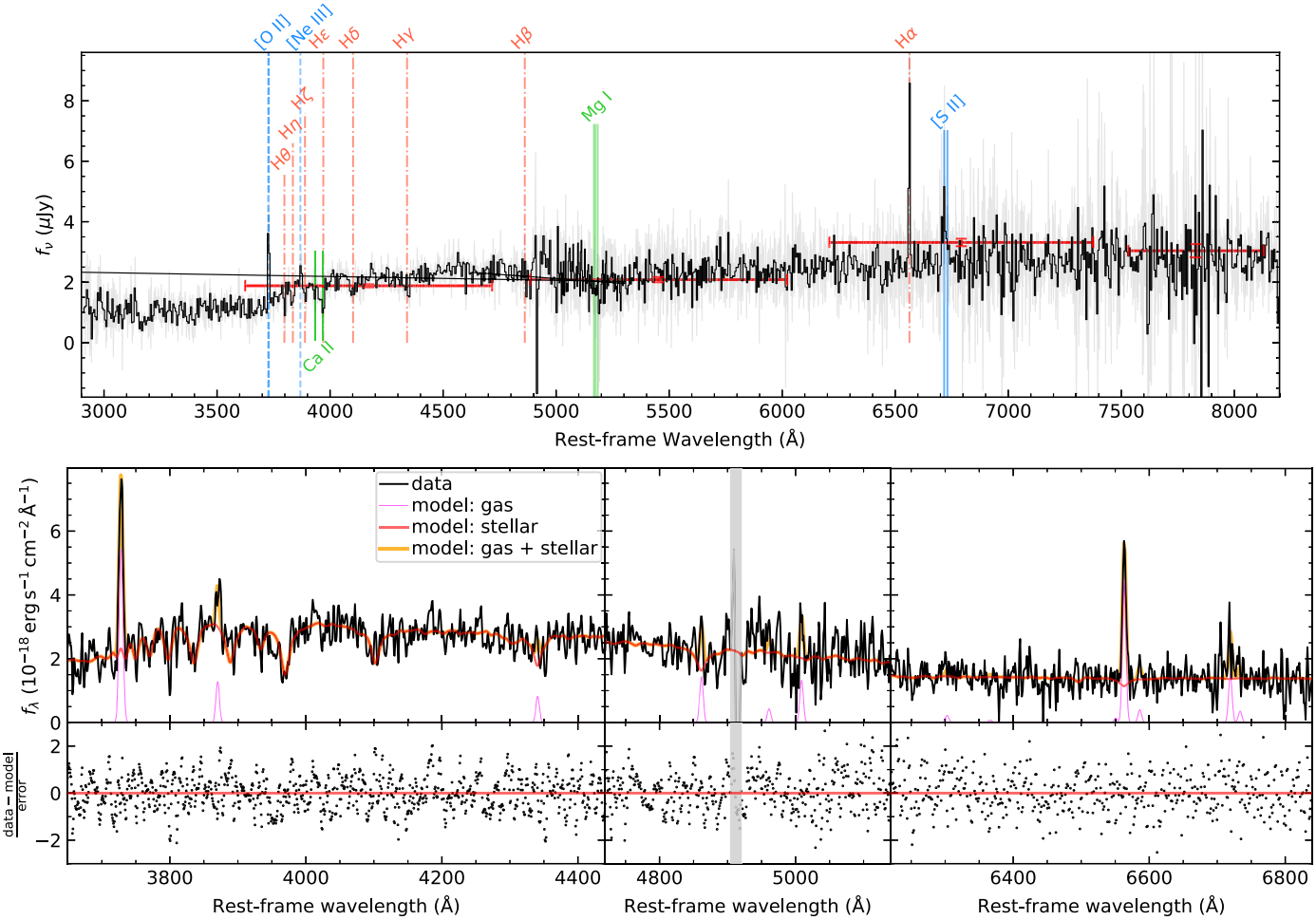

Figure 9. *Upper panel*: spectrum (corrected for Galactic extinction) of the host galaxy, overplotted with HSC *griz* photometry. *Bottom panel*: zoomed-in regions of the spectrum (black lines, corrected for Galactic extinction). The thick orange lines show the best-fit `ppxf` model, which is a combination of the stellar continuum (red lines) and emission lines (thin magenta lines). The rest-frame wavelength range 4904–4920 Å is masked due to the large uncertainty of f_λ (contamination by a sky line).

Table 4
Observed Photometry of the Host Galaxy

Instrument	Band	$\lambda_{\rm eff}$ (Å)	Magnitude
GALEX	FUV	1528	>23.276
GALEX	NUV	2271	>23.579
HSC	*g*	4755	23.282 ± 0.029
HSC	*r*	6184	23.152 ± 0.046
HSC	*i*	7661	22.635 ± 0.040
HSC	*z*	8897	22.721 ± 0.079
HSC	*y*	9762	22.359 ± 0.133

Note. The HSC Kron radius is 0.″705. GALEX upper limits are given in 3σ.

Table 5
Galactic Extinction Corrected Galaxy Emission Line Fluxes

Line	Flux (10^{-18} erg s^{-1} cm^{-2} Å^{-1})
[O II] $\lambda\lambda$3726, 3729	53.00 ± 6.09
[Ne III] λ3869	10.96 ± 1.97
Hγ λ4340	6.31 ± 1.55
Hβ λ4861	9.81 ± 1.87
[O III] $\lambda\lambda$4959, 5007	11.67 ± 4.57 (2.6σ)
[O I] $\lambda\lambda$6300, 6364	1.59 ± 1.17 (1.4σ)
Hα λ6563	22.82 ± 0.89
[N II] $\lambda\lambda$6548, 6583	2.72 ± 1.71 (1.6σ)
[S II] λ6716	7.32 ± 2.01
[S II] λ6731	1.77 ± 1.26 (1.4σ)

Note. Marginally detected emission lines are indicated with the detection significance shown in the parenthesis.

we obtain $\log(M_*/M_\odot) = 7.94^{+0.22}_{-0.39}$, $\log(Z/Z_\odot) = -0.46^{+0.20}_{-0.17}$, $\tau_{\rm SFH} = 11.6^{+45.6}_{-10.0}$ Gyr, $t_{\rm age} = 1.82^{+4.07}_{-1.50}$ Gyr, and $E(B-V)_{\rm host} = 0.21^{+0.10}_{-0.12}$, where uncertainties are epresented by the 68% confidence intervals.

Using the 90% confidence interval of the M_* posterior probability function and the mass–metallicity relation (MZR) of low-mass galaxies (Berg et al. 2012), we infer that the typical $\log(Z/Z_\odot)$ at the host mass should be $-0.78^{+0.10}_{-0.16} \pm 0.15$(sys). The measured metallicity is therefore on the high end of the distribution.

We convolve the observed LRIS spectrum with the HSC *i*-band filter and compare the flux with the host photometry (Table 4), which suggests that 80.6% of the total host flux is captured by the LRIS slit. Subsequently, we assume the same fraction of total Hα flux is captured by the slit and no host extinction, and calculate the Hα luminosity to be $L_{\rm H\alpha} = (1.39 \pm 0.05) \times 10^{39}$ erg s^{-1}. Using the Kennicutt

Table 6
Emission Line Ratios

Definition	Value
[O III]λ5007/Hβ	$0.90^{+0.78}_{-0.58}$
log{[O III]λ5007/Hβ}	$-0.05^{+0.27}_{-0.45}$
[N II] λ6583/Hα	<0.18
N2 $\equiv$ log{[N II] λ6583/Hα}	<-0.73
O3N2 $\equiv$ log{[O III]λ5007/Hβ}$-$N2	<-1.71
[S II] $\lambda\lambda$6716,31/Hα	0.40 ± 0.17
log{[S II] $\lambda\lambda$6716,31/Hα}	$-0.40^{+0.16}_{-0.24}$
[O I] λ6300/Hα	< 0.12
log{[O I] λ6300/Hα}	<-0.94

Note. Line ratios and their uncertainties are estimated using the 5th, 50th, and 95th percentiles of the MC simulations. When the 5th percentile value is negative, we present the 95th percentile as an upper limit.

(1998) relation converted to a Chabrier initial mass function (Chabrier 2003; Madau & Dickinson 2014), we infer a star formation rate (SFR) of $(6.93 \pm 0.27) \times 10^{-3}\,M_\odot\,\mathrm{yr}^{-1}$. An extinction of $E(B-V)_{\rm host} \sim 0.21$ will render the SFR higher by a factor of $\sim$1.5. Therefore, hereafter we adopt $\mathrm{SFR} = 6.93^{+3.90}_{-0.27} \times 10^{-3}\,M_\odot\,\mathrm{yr}^{-1}$. The specific star formation rate is $\mathrm{sSFR} \equiv \mathrm{SFR}/M_* = 0.80^{+0.45}_{-0.03} \times 10^{-10}\,\mathrm{yr}^{-1}$, where we only consider the uncertainty of SFR but exclude the uncertainty of M_*.

3. Inferences and Discussion

3.1. A Mildly Relativistic Shock in a Dense Environment

3.1.1. Standard SSA Modeling

At $\Delta t \approx 261$ days, the observed spectral index of $\beta_2 \approx -1$ (Section 2.6) in the optically thin regime of the radio SED motivates us to adopt the standard model given by Chevalier (1998), where the electrons in the CSM are accelerated by the forward shock into a power-law distribution of energy $N(E) = N_0 E^{-p}$. We do not consider the alternative of a relativistic Maxwellian electron-energy distribution, in which case we expect a much steeper β_2 (see, e.g., Figure 11 of Ho et al. 2021b) and a shock speed of $v_{\rm sh} \gtrsim 0.2c$ (Margalit & Quataert 2021). The $v_{\rm sh}$ inferred from our observations is much slower (see below). We note that the standard model might not be fully appropriate because the observed spectral index of β_1 in the optically thick regime is much shallower than the $\beta_1 = 2.5$ expected from SSA. We investigate the effects of CSM inhomogeneity and scintillation in Section 3.1.2.

In the standard model of Chevalier (1998), the minimum electron energy is $E_{\rm min} = 511$ keV; the peak of the SED is governed by synchrotron self-absorption (SSA) such that $\tau(\nu_{\rm peak}) = 1$; the radio emitting region is approximated by a sphere with radius R and volume filling factor f (hereafter assumed to be 0.5); the magnetic energy density ($U_B \propto B^2$) and the relativistic electron energy density ($U_e \propto N_0$) are assumed to scale as the total (thermalized) post-shock energy density U, such that $U_B = \epsilon_B U$ and $U_e = \epsilon_e U$.

We define $L_{\theta\nu} \equiv 4\pi D_\theta^2 f_\nu = L_\nu/(1+z)^4$, $L_{\theta\nu,29} \equiv L_{\theta\nu,\rm peak}/(10^{29}\,\mathrm{erg\,s^{-1}\,Hz^{-1}})$ and $\nu_5 \equiv \nu_{\rm peak}/(5\,\mathrm{GHz})$, such that

$$R = 7.1 \times 10^{16} \left(\frac{\epsilon_e}{\epsilon_B}\right)^{-1/19} L_{\theta\nu,29}^{9/19} \nu_5^{-1}\,\mathrm{cm} \quad (3a)$$

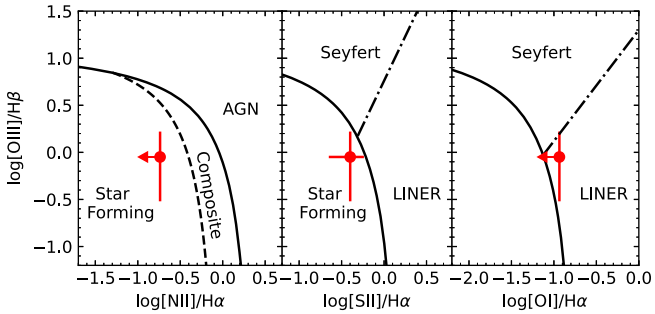

Figure 10. The host galaxy of AT2020mrf on the BPT diagrams. The diagnostic lines follow Figure 4 of Kewley et al. (2006).

$$B = 0.36 \left(\frac{\epsilon_e}{\epsilon_B}\right)^{-4/19} L_{\theta\nu,29}^{-2/19} \nu_5\,\mathrm{G} \quad (3b)$$

$$U = 4.0 \times 10^{48} \frac{1}{\epsilon_B} \left(\frac{\epsilon_e}{\epsilon_B}\right)^{-11/19} L_{\theta\nu,29}^{23/19} \nu_5^{-1}\,\mathrm{erg}. \quad (3c)$$

The upstream CSM density can be estimated under the conditions of strong shocks and fully ionized hydrogen (see Equation (16) of Ho et al. 2019):

$$n_e = 61 \frac{1}{\epsilon_B} \left(\frac{\epsilon_e}{\epsilon_B}\right)^{-6/19} L_{\theta\nu,29}^{-22/19} \nu_5^4 \left(\frac{\Delta t}{100\,\mathrm{days}}\right)^2 \mathrm{cm}^{-3} \quad (4)$$

Assuming that the CSM density profile is determined by a pre-explosion steady wind with mass-loss rate $\dot{M}$ and velocity $v_{\rm w}$, we have (see Equation (23)[14] of Ho et al. 2019):

$$\frac{\dot{M}}{v_{\rm w}} \left(\frac{1000\,\mathrm{km\,s^{-1}}}{10^{-4}\,M_\odot\,\mathrm{yr}^{-1}}\right) = 0.10 \left(\frac{1}{\epsilon_B}\right) \left(\frac{\epsilon_e}{\epsilon_B}\right)^{-8/19} \times L_{\theta\nu,29}^{-4/19} \nu_5^2 \left(\frac{\Delta t}{100\,\mathrm{days}}\right)^2 \quad (5)$$

We adopt $L_{\theta\nu\,\rm peak} = L_{\nu\,\rm peak}/(1+z)^4 \approx 1.0 \times 10^{29}\,\mathrm{erg\,s^{-1}\,Hz^{-1}}$ and $\nu_{\rm peak} \approx 7$ GHz at $\Delta t = 261$ days. Assuming $\epsilon_e = \epsilon_B = 1/3$, we have $R \approx 5.1 \times 10^{16}$ cm, $B \approx 0.50$ G, $U \approx 1.7 \times 10^{49}$ erg, and $n_e \approx 3.5 \times 10^3\,\mathrm{cm^{-3}}$. Assuming $\epsilon_e = 0.1$, $\epsilon_B = 0.01$, we have $R \approx 4.6 \times 10^{16}$ cm, $B \approx 0.31$ G, $U \approx 1.5 \times 10^{50}$ erg, and $n_e \approx 5.6 \times 10^4\,\mathrm{cm^{-3}}$. The average shock velocity ($v_{\rm sh} = R/\Delta t$) is 0.07–0.08c, suggesting a mildly relativistic shock. The derived R, U, $v_{\rm sh}$ should be taken as upper limits, B, n_e, $\dot{M}/v_{\rm w}$ should be taken as upper limits. See the discussion in Section 3.1.2.

The upper panel of Figure 11 compares AT2020mrf with normal SNe (Bietenholz et al. 2021), SNe associated with long GRBs, and four AT2018cow-like objects in the literature. Note that all GRB-SNe are of type Ic-BL. The peak luminosity of AT2020mrf is much greater than normal SNe and is in the same regime as other AT2018cow-like objects. A physical interpretation is that the energy divided by the shock radius ($\mathrm{U/R} \propto L_{\theta\nu\,\rm peak}^{14/19}$) is greater. This indicates a more efficient conversion/thermalization of energy, which can come from a higher explosion energy or a higher ambient density (Ho et al. 2019).

Moreover, we see that the CSM "surface density" ($n_e R^2 \propto \dot{M}/v_{\rm w}$) of AT2020mrf at 261 days is similar to AT2018cow at 22 days. At a similar shock radius of

[14] The normalization constant in Equation (23) of Ho et al. 2019 is off by a factor of $\sim$10. Here we update the equation with the correct constant.

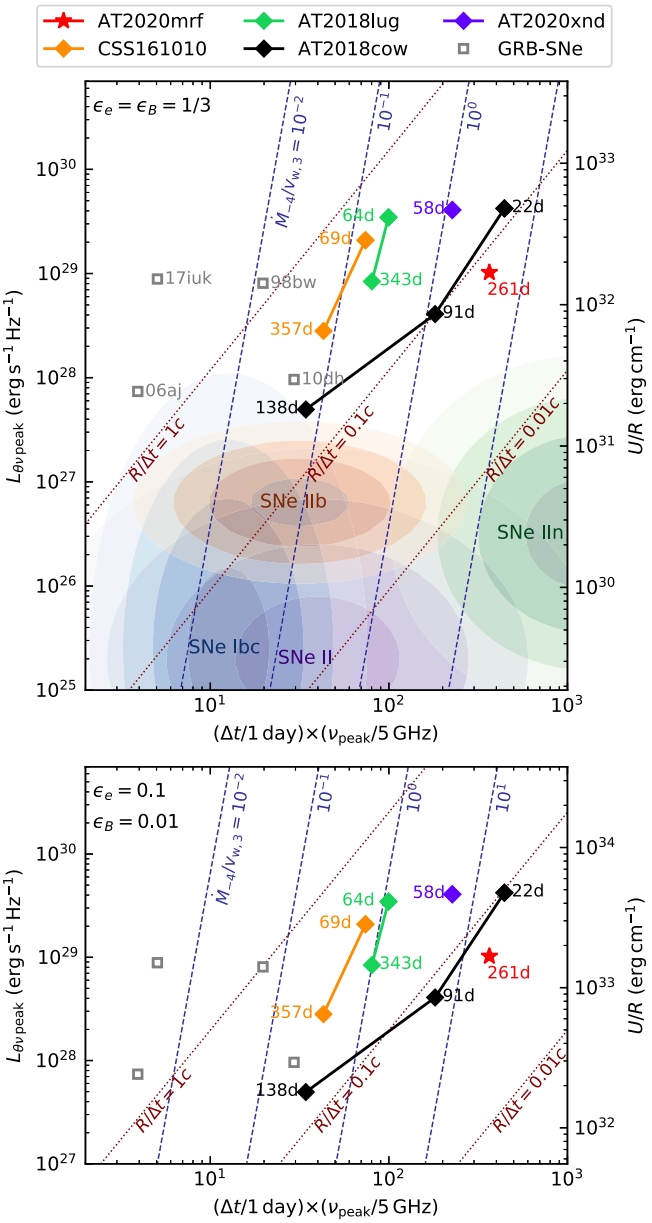

Figure 11. Peak radio luminosity ($L_{\nu\,\mathrm{peak}}$) vs. the product of peak time and ν_{peak}. Under the assumptions of the standard SSA model, dotted lines mark constant time-averaged velocity; Dashed lines mark constant mass-loss rate ($\dot{M}_{-4} \equiv \dot{M}/(10^{-4}\,M_\odot\,\mathrm{yr}^{-1})$) scaled to wind velocity ($v_{\mathrm{w},3} \equiv v_{\mathrm{w}}/(10^3\,\mathrm{km\,s}^{-1})$). The two panels show the results with different assumptions of ϵ_e and ϵ_B. The data of AT2018cow-like objects and GRB-SNe are based on Figure 9 of Ho et al. (2021b) and Figure 3 of Nayana & Chandra (2021).

$R \sim 6 \times 10^{16}$ cm, the CSM number density of AT2018cow is $n_e < 33\,\mathrm{cm}^{-3}$ (Nayana & Chandra 2021)—which is more than 100 times smaller than that in AT2020mrf. Since $\dot{M}/v_{\mathrm{w}}$ generally decreases at later times (i.e., the density profile is steeper than $n_e \propto r^{-2}$), the immediate environment of AT2020mrf is probably denser than all other AT2018cow-like events.

3.1.2. CSM Inhomogeneity and Scintillation

The small values of β_1 and the flat-topped radio SEDs (Figure 8) motivate us to assume an inhomogeneous CSM, which means that the distribution of electrons or magnetic field strength varies within the synchrotron source (Björnsson &

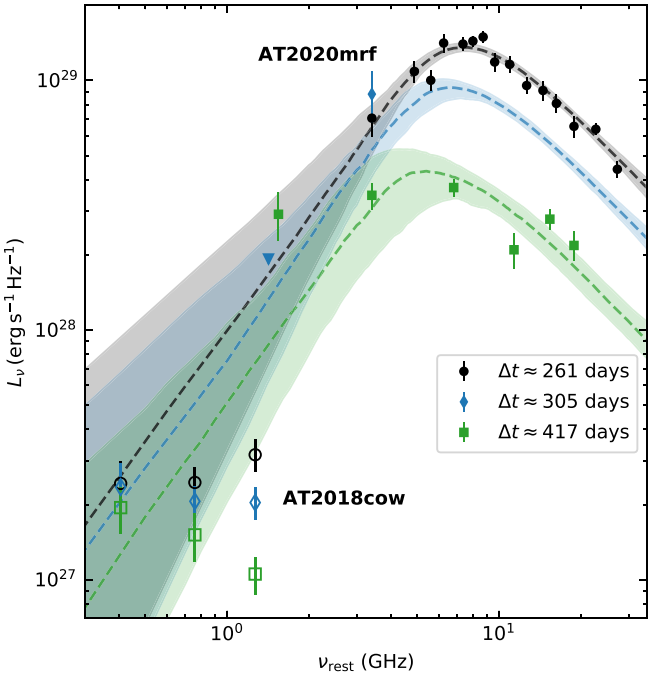

Figure 12. Radio SEDs of AT2020mrf (solid markers), compared with the that of AT2018cow at similar phases (hollow markers, interpolated from Table 1 of Nayana & Chandra 2021). Dashed lines are the inhomogeneous SSA model fits to the observations of AT2020mrf.

Keshavarzi 2017). In this model, between the standard SSA optically thick $F_\nu \propto \nu^{5/2}$ regime and the optically thin $F_\nu \propto \nu^{-(p+1)/2}$ regimes, there is a transition regime with a spectral index of $0 < \beta < 2.5$. Since the measured β_1 remains below 2.5, we assume that the standard SSA optically thick regime is at frequencies lower than our observations.

Following Chandra et al. (2019), we fit the full set of radio data with the function

$$L(\nu, t) = K_1 \nu_5^{\beta} \left(\frac{\Delta t}{100\ \mathrm{days}}\right)^{a} [1 - \exp(-\tau_{\mathrm{ssa}}(\nu, t))], \quad (6)$$

where τ_{ssa} is the SSA optical depth

$$\tau_{\mathrm{ssa}}(\nu, t) = K_2 \nu_5^{-(\beta + \frac{p-1}{2})} \left(\frac{\Delta t}{100\ \mathrm{days}}\right)^{-(a+b)}. \quad (7)$$

The best-fit model is shown in Figure 12, with $K_1 = 5.4^{+14.6}_{-4.4} \times 10^{29}\,\mathrm{erg\,s^{-1}\,Hz^{-1}}$, $K_2 = 13^{+53}_{-10}$, $\beta = 1.6^{+0.8}_{-0.6}$, $p = 3.3^{+0.4}_{-0.3}$, $a = -1.6^{+1.8}_{-1.4}$, and $b = 3.0^{+0.3}_{-0.4}$. Evidence of source inhomogeneities has also been found in AT2018cow (Nayana & Chandra 2021). With an inhomogeneous CSM, the R, U, and v_{sh} values derived in Section 3.1.1 should be taken as lower limits, and B, n_e, and $\dot{M}/v_{\mathrm{w}}$ should be taken as upper limits.

A few data points at $\Delta t > 300$ days are not well fitted by the inhomogeneous SSA model. We estimate the effects of interstellar scintillation (ISS) to our radio observations using the NE2001 model (Cordes & Lazio 2002) of the Galactic distribution of free electrons. The transition frequency below which strong scattering occurs is (Goodman 1997):

$$\nu_{\mathrm{ss}} = 10.4(\mathrm{SM}_{-3.5})^{6/17} d_{\mathrm{scr,kpc}}^{5/17}\ \mathrm{GHz}, \quad (8)$$

where $\mathrm{SM}_{-3.5} \equiv \mathrm{SM}/(10^{-3.5}\,\mathrm{m}^{-20/3}\,\mathrm{kpc})$ is the scintillation measure, and $d_{\mathrm{scr,kpc}}$ is the distance to the electron scattering

screen in kpc. For the line of sight to AT2020mrf (Galactic coordinates $l = 71.^{\circ}339$, $b = 50.^{\circ}806$), NE2001 predicts $\nu_{ss} = 8.3$ GHz and $SM_{-3.5} = 0.53$, implying $d_{scr,kpc} = 1.0$. This suggests that the 11.35 GHz "dip" (or 15–19 GHz "excess") cannot be explained by ISS.

AT2020mrf is subject to diffractive or refractive ISS if the source angular size satisfies $\theta_s < 3.3\nu_{10}^{6/5}$ μas or $\theta_s < 2.0\nu_{10}^{-11/5}$ μas (Goodman 1997). We have shown that the shock radius at times of our radio observations is $R \gtrsim 5 \times 10^{16}$ cm, corresponding to $\theta_s \gtrsim 6.8$ μas. Therefore, the 3.4 GHz "excess" at $\Delta t \approx 305$ days and the 1.5 GHz "excess" at $\Delta t \approx 417$ days are likely caused by refractive ISS.

3.2. Properties of the Optical Emission

3.2.1. Rise and Decline Timescales

To constrain the optical evolution of AT2020mrf around maximum, we model the multi-band photometry using a power-law rise and an exponential decay. For simplicity we assume a blackbody SED and a single temperature for data at $\Delta t < 15$ days. The best-fit model in the r_{ZTF} band is shown as the solid orange line in Figure 1.

To compare AT2020mrf with the sample of spectroscopically classified FBOTs presented by Ho et al. (2021a), we calculate the time it takes for AT2020mrf to rise from half-max to max ($t_{1/2,rise} = 2.4 \pm 0.2$ days) and to decline from max to half-max ($t_{1/2,fade} = 4.8 \pm 0.2$ days). Its total duration above half-max is $t_{1/2} = 7.1^{+0.3}_{-0.2}$ days. On the M_{peak} versus $t_{1/2}$ diagram (see, e.g., Figure 1 of Ho et al. 2021a and Figure 7 of Perley et al. 2022), AT2020mrf lies between previously studied AT2018cow-like events ($t_{1/2} \lesssim 5$ days, $M_{peak} \lesssim -20.5$) and interacting SNe of type IIn/Ibn/Icn ($t_{1/2} \gtrsim 7$ days, $M_{peak} \gtrsim -20.0$).

3.2.2. Color Evolution

The $g - r$ color of AT2020mrf is -0.34 ± 0.20 mag at the day of discovery ($\Delta t \approx 0.25$ day), and reddens at later times. At $\Delta t \approx 6.4$, 11.7, and 23–28 days, the $g - r$ values are -0.05 ± 0.06 mag, -0.09 ± 0.14 mag, and 0.05 ± 0.27 mag, respectively. Assuming that the optical SED can be modeled by a blackbody, the blackbody temperature (T_{bb}) decreases from $\sim 2 \times 10^4$ K to $\sim 10^4$ K. Similar cooling signatures have also been observed in AT2018lug, while both AT2018cow and AT2020xnd remain blue post-peak.

Figure 13 compares the color evolution of AT2020mrf with other FBOTs. We have included AT2018cow (Perley et al. 2019), AT2018lug (Ho et al. 2020), AT2020xnd (Perley et al. 2021), the type Icn SNe 2019hgp (Gal-Yam et al. 2022) and 2021csp (Perley et al. 2022), as well as the gold sample of 22 spectroscopically classified FBOTs presented by Ho et al. (2021a). The calculated $g - r$ color has been corrected for Galactic extinction but assumes no host reddening. As can be seen, the amount of $g - r$ increase observed in AT2020mrf is closer to other multi-wavelength FBOTs and interacting SNe, but smaller than events shown in the lower panels.

3.2.3. Possible Power Sources

Like many other FBOTs, the fast rise and luminous optical peak of AT2020mrf is unlikely to be powered by radioactive ^{56}Ni decay, which would require the nickel mass M_{Ni} to be greater than the ejecta mass M_{ej} (see, e.g., Figure 1 of Kasen 2017). Possible emission mechanisms include shock breakout (SBO) from extended CSM (Waxman & Katz 2017), shock cooling emission (SCE) from an extended envelope (Piro et al. 2021), continued interaction between the SN ejecta and the CSM (Smith 2017; Fox & Smith 2019), and reprocessing of X-ray/UV photons (potentially deposited by a central engine) by dense outer ejecta (Margutti et al. 2019) or an optically think wind (Piro & Lu 2020). We do not attempt to distinguish between these scenarios due to a lack of multi-wavelength observations at early times.

The decay rate of AT2020mrf is significantly slower than that of AT2018cow and AT2020xnd (Figure 1). This is similar to the post-peak decay of AT2018lug, which also slows down at $\Delta t \approx 6$–8 days (see Figure 1). The slower decay can be caused either by the emergence of a radioactivity powered SN or continued CSM interaction. Since the color evolution of AT2020mrf is most similar to interacting SNe shown in the upper right-hand panel of Figure 13, we slightly favor the CSM interaction scenario. In Appendix C, we attempt to fit the multi-band light curve using the one-zone SBO+SCE model presented by Margalit (2021), but no satisfactory fit is obtained. However, given that the CSM interaction model has many free parameters (e.g., anisotropy, radial density structure), more detailed modeling would be required to determine if it is a viable emission mechanism.

Assuming $T_{bb} = 10^4$ K, the bolometric luminosity and blackbody radius of AT2020mrf are shown in Figure 14. Although radioactivity is not required to explain the optical emission, the light curve at $\Delta t \gtrsim 10$ days is consistent with being dominated by nickel decay with $M_{ej} \sim 1$–$6\,M_{\odot}$ and $M_{Ni} \sim 0.3$–$0.4\,M_{\odot}$. Improved analytic relations (compared to the "Arnett model" shown in Figure 14) have been presented by Khatami & Kasen (2019). Adopting $L_{peak} \approx 10^{42.8}$, $t_{peak} \approx 17$ days, and the dimensionless parameter $\beta \approx 1$, we use Equation (21) of Khatami & Kasen (2019) to estimate M_{Ni}, which gives $M_{Ni} \approx 0.26\,M_{\odot}$. In summary, the inferred M_{ej} and M_{Ni} are broadly consistent with stripped-envelope SNe of all types (IIb, Ib, Ic, and Ic-BL; Drout et al. 2011; Taddia et al. 2018; Prentice et al. 2019), but cannot accommodate normal hydrogen-rich type II SNe (Meza & Anderson 2020; Afsariardchi et al. 2021).

3.3. A Dwarf Host Galaxy

Figure 15 shows the position of AT2020mrf on the SFR–M_* and the sSFR–M_* diagrams (based on properties derived in Section 2.7.2). For comparison, we also show the 28 FBOTs selected from ZTF (note that we excluded the three 18cow-like events from the 31 objects in Table 17 of Ho et al. 2021a), the 49 rapidly evolving transients (RETs) from the dark energy survey (DES) (Wiseman et al. 2020), and 18 PTF SLSNe-I from Perley et al. (2016a). Compared with normal CCSNe (Schulze et al. 2021) and X-ray/radio-faint FBOTs, the M_* of AT2018cow-like events (a sample of five) is much smaller. Indeed, all AT2018cow-like events are hosted by dwarf galaxies with $M_* < 2 \times 10^9\,M_{\odot}$. This trend has been previously reported by Perley et al. (2021), and argues for a massive star origin. Several types of the most powerful explosions from massive stars are also preferentially hosted by dwarf galaxies, including long GRBs (Vergani et al. 2015; Perley et al. 2016b), hydrogen-poor SLSNe (Leloudas et al. 2015; Perley et al. 2016a; Taggart & Perley 2021), and SNe Ic-BL (Schulze et al. 2021).

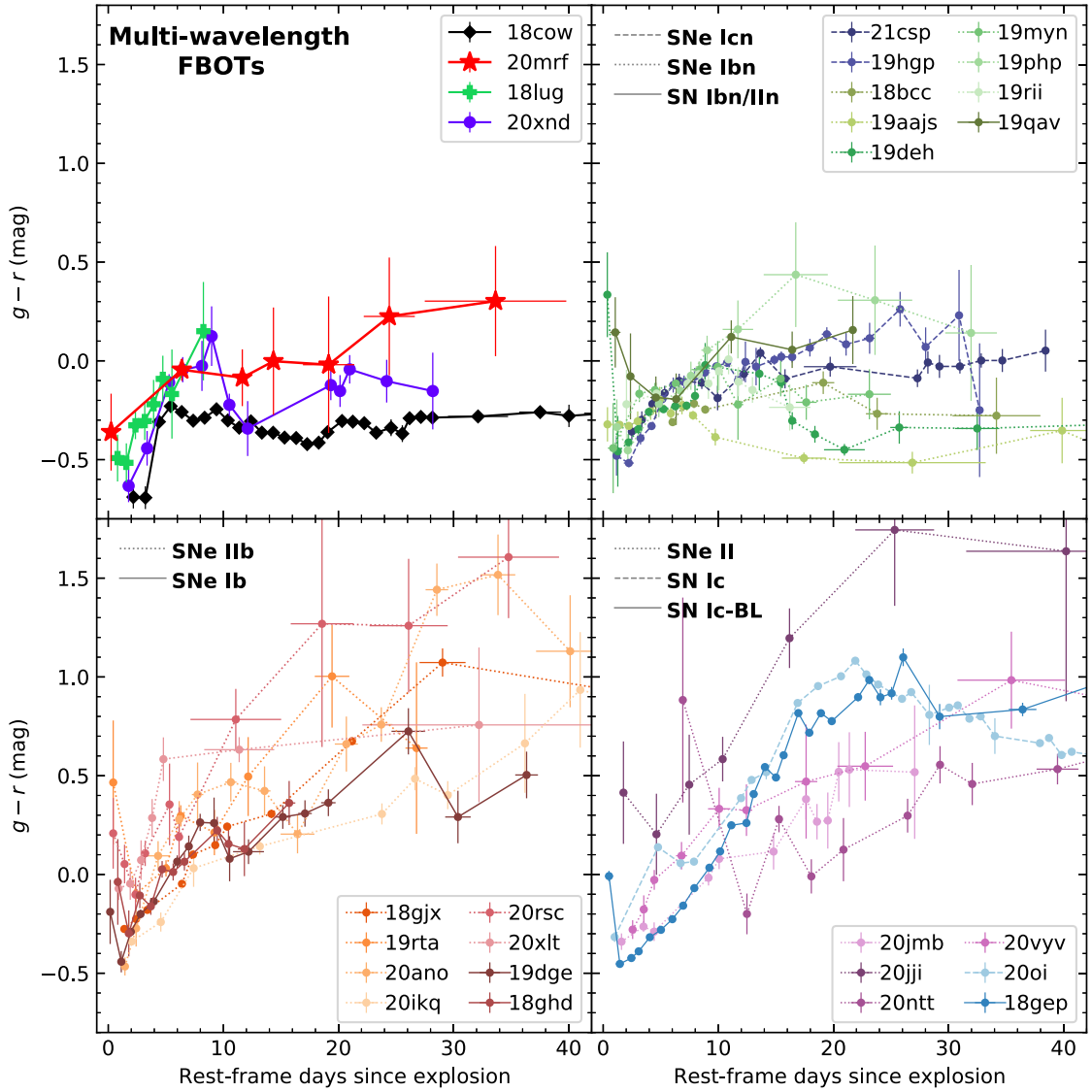

Figure 13. Color evolution of FBOTs. The upper left-hand panel shows four events associated with bright radio emission. The upper right-hand panel shows interacting SNe of type Icn, Ibn, and IIn. The lower panels show type II SNe, as well as stripped-envelope SNe of type IIb, Ib, Ic, and Ic-BL.

Perley et al. (2021) have suggested that an elevated level of SFR or sSFR is not a requirement for producing AT2018cow and similar explosions. The properties of AT2020mrf's host further support this suggestion. At $M_* \sim 10^8\,M_\odot$, the SFR of AT2020mrf lies below the main-sequence (MS) of local star-forming galaxies. Moreover, among the 369 PTF/iPTF normal CCSNe hosted by galaxies with $M_* < 2 \times 10^9\,M_\odot$ (Schulze et al. 2021), the host galaxies of only 30 objects (8%) have sSFR $< 8 \times 10^{-11}\,\mathrm{yr}^{-1}$. This indicates that AT2020mrf does not occur during a vigorous starburst and that progenitor scenarios with a slightly longer delay time than that of a typical CCSN are favored. Zapartas et al. (2017) performed a population synthesis study of CCSNe, finding that a prolonged delay time can be achieved by binary interactions through common envelope evolution, mass transfer episodes, and/or merging. Explosions driven by the merging of a compact object with a massive star inside a common envelope have indeed been proposed as promising channels for producing AT2018cow-like events (Soker et al. 2019; Schrøder et al. 2020; Soker 2022; Metzger 2022).

Among the five AT2018cow-like events, only AT2018lug lies above the local MS of star-forming galaxies. For comparison, the majority (15/18) of SLSNe-I presented by Perley et al. (2016a) lie above the local MS.[15] We perform a two-sided Kolmogorov–Smirnov (K-S) test for the null hypothesis that the host galaxy sSFR of SLSNe-I and AT2018cow-like events are drawn from the same distribution. The returned p-value of 0.23 is too high to reject the null hypothesis. A larger sample size is clearly needed to test if the host sSFR between AT2018cow-like events and other powerful massive star explosions are statistically different.

3.4. An Engine-driven Explosion

3.4.1. X-Ray Properties

We have shown that the radio (Section 3.1) and early-time optical (Sections 2.2, 3.2) properties of AT2020mrf are similar to other AT2018cow-like events. Here, we summarize the key

[15] Compared with AT2018cow-like events, the sample of SLSNe-I is at slightly higher redshifts (the median is $z \sim 0.2$). We note that for $M_* \approx 10^8\,M_\odot$, the sSFR at $z \approx 0.2$ is only slightly (≈0.2 dex) higher than that at $z \approx 0$ (Speagle et al. 2014).

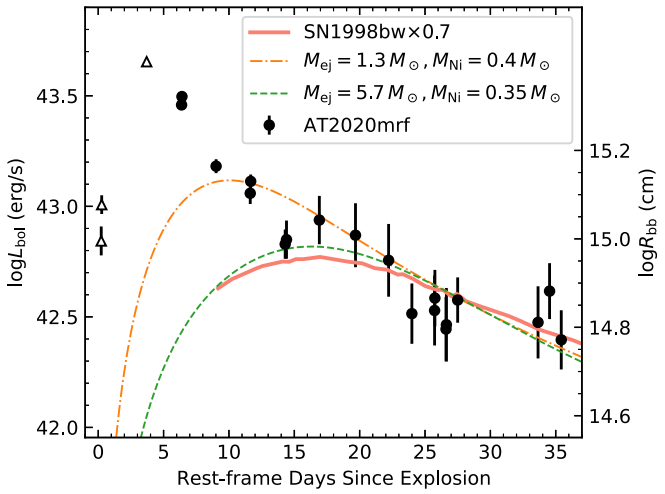

Figure 14. Bolometric light curve of AT2020mrf converted from ZTF photometry, assuming $T_{bb} = 10^4$ K. Data at <5 days are shown as upward triangles because the temperature at early time is $>10^4$ K. The L_{bol} of SN1998bw (Galama et al. 1998) is shown for comparison. We show two models of radioactivity powered SN in the photospheric phase (Valenti et al. 2008; Lyman et al. 2016), adopting an opacity of $\kappa = 0.07$ cm^2 g^{-1} (typical for stripped-envelope SNe; Taddia et al. 2018), and a photospheric velocity of $v_{phot} = 2 \times 10^4$ km s^{-1} (typical for GRB-SNe; Modjaz et al. 2016).

X-ray observables of AT2020mrf, and compare them with other AT2018cow-like events.

At ∼36 days, the mean 0.3–10 keV luminosity of AT2020mrf is $(1.9 \pm 0.4) \times 10^{43}$ erg s^{-1}, a factor of ∼20 brighter than AT2018cow and AT2020xnd at similar phases (Figure 7). The best-fit power law of $f_\nu \propto \nu^{-0.8}$ (Figure 5) is similar to the 0.3–10 keV spectral shape of AT2018cow and AT2020xnd (Margutti et al. 2019; Bright et al. 2022; Ho et al. 2021b). From 34.5 to 37.6 days, the 0.2–2.2 keV flux varies by a factor of ≈6 on the timescale of ≈1 day (Figure 4), which is similar to the fast soft X-ray variability observed in AT2018cow at similar phases (Figure 7).

At 328 days, the mean 0.3–10 keV luminosity of AT2020mrf is $\sim 1.4 \times 10^{42}$ erg s^{-1}, which is ∼300 times brighter than the upper limit of CSS161010 at 291 days, and ∼200 times brighter than AT2018cow itself at 212 days. The spectrum of AT2020mrf has probably hardened to $f_\nu \propto \nu^0$. From 327.4 to 328.2 days, the X-ray flux decreases by a factor of ∼2.6.

Among AT2018cow-like events, intraday X-ray variability has only been detected in AT2018cow and AT20202mrf. This is probably because CSS161010, AT2018lug, and AT2020xnd were not observed often enough to detect it. The isotropic equivalent observed X-ray luminosity of AT2020mrf is as luminous as long GRBs. The X-ray emission of long GRBs are produced by the afterglow synchrotron radiation of electrons accelerated by a ultra-relativistic shock (Sari et al. 1998). However, given the lack of a prompt γ-ray emission (Section 2.5) and the sub-relativistic shock velocity (Section 3.1) observed in AT2020mrf, the nature of its X-rays should be different from that of long GRBs.

As shown in Figure 7, in AT2018cow (and perhaps AT2020xnd), the 0.3–10 keV light-curve decay steepens from $L \propto t^{-1}$ ($t \lesssim 25$ days) to $L \propto t^{-4}$ ($25 \lesssim t \lesssim 100$ days). The overall decay shape of AT2020mrf is consistent with a $L \propto t^{-1.3}$ power law. However, we cannot rule out the existence of a steeper decay (see Section 3.4.3). Below we discuss the physical origin of the X-ray emission associated with AT2020mrf.

3.4.2. General Considerations

First, Figure 16 shows that the late-time X-ray luminosity of AT2020mrf is too bright to be an extension of the radio synchrotron spectrum.

Second, inverse-Compton (IC) scattering of the radiation field (i.e., UV/optical photons) by electrons accelerated in the forward shock is found to be the main early-time ($t \lesssim 40$ days) X-ray emission mechanism for SNe Ib/c exploding in low-density environments (Fransson et al. 1996; Kamble et al. 2016). The ratio of IC to synchrotron radiation losses is $P_{IC}/P_{syn} = u_{rad}/u_B$, where u_{rad} is the energy density in seed photons, and $u_B = U_B/(4\pi R_{sh}^3/3)$. To first order, $P_{IC}/P_{syn} \sim L_X/L_{radio}$. At $\Delta t \approx 36$ days, the bolometric luminosity of the optical transient is $L_{bol} \sim 10^{42.3}$ erg s^{-1} (see Figure 14). Assuming $v_{sh} \sim 0.07$–$0.08c$ (Section 3.1.1), the shock radius is $R_{sh} \sim 7 \times 10^{15}$ cm. Therefore, $u_{rad}/L_X = L_{bol}/(4\pi c R_{sh}^2)/L_X \sim (0.1\ \mathrm{erg\ cm^{-3}})/(2 \times 10^{43}\ \mathrm{erg\ s^{-1}}) \sim 5.4 \times 10^{-45}$ s cm^{-3}. Assuming that the standard SSA model applies at $\Delta t \approx 36$ days,[16] from Equation (3c), we have $u_B/L_{radio} \sim 8 \times 10^{-31} L_{\theta\nu,29}^{4/19} (\epsilon_e/\epsilon_B)^{-11/19} \nu_{100}^{-1} > 2 \times 10^{-31}$ s cm^{-3}, where we have assumed that the early-time synchrotron emission peaks at ∼100 GHz and $L_{\theta\nu} > 10^{29}$ erg s^{-1} Hz^{-1}. Therefore, $u_{rad}/L_X \ll u_B/L_{radio}$, and IC is not likely to be the dominant mechanism for the X-ray emission. At $\Delta t \approx 328$ days, the observed X-ray spectral shape of $f_\nu \propto \nu^0$ is too hard to be consistent with IC.

Finally, X-rays from most normal CCSNe and interacting SNe have been successfully modeled by thermal bremsstrahlung from supernova reverse-shock-heated ejecta or the forward-shock-heated CSM (Chevalier & Fransson 1994; Dwarkadas & Gruszko 2012). The shortest variability timescale that is expected from clumpy CSM encountered by a forward shock is much slower—$\Delta t/t = v_{sh}/c \sim 0.1$ (see Section 3.3.1 of Margutti et al. 2019). In contrast, the X-ray relative variability and flux contrast are $\Delta t/t \approx 0.03$, $\Delta F/F \approx 2.5$ at $t \approx 36$ days and $\Delta t/t \lesssim 0.003$, $\Delta F/F \approx 1$ at $t \approx 328$ days.

Some previous studies have interpreted AT2018cow as the tidal disruption of a white dwarf or star by an IMBH (Kuin et al. 2019; Perley et al. 2019). Since the observed early-time non-thermal X-ray spectrum and fast variability are not consistent with observations of thermal X-ray loud TDEs (Sazonov et al. 2021), the X-rays are thought to be powered by a jet similar to that observed in the jetted TDE SwiftJ1644 (Burrows et al. 2011; Bloom et al. 2011). However, for AT2020mrf and AT2018cow-like events in general, the TDE scenario is disfavored by the dense environment (Section 3.1) and the host properties (Section 3.3).

Therefore, the most natural origin of the X-rays in AT2020mrf is a central compact object—either a neutron star (Section 3.4.4) or a black hole (Section 3.4.3)—formed in a massive star explosion. Since the UV/optical luminosity of AT2020mrf remains much lower than L_X throughout the evolution, we can assume that the central engine luminosity L_e is mostly tracked by L_X. The engine timescale is set by the duration of the X-ray emission $t_e > 328$ days. The total energy release in the X-ray is $E_e > (2 \times 10^{43}\ \mathrm{erg\ s^{-1}}) \times (36\ \mathrm{days}) + (10^{42}\ \mathrm{erg\ s^{-1}}) \times [(328 - 36)\mathrm{days}] = 9 \times 10^{49}$ erg.

[16] This assumption will not be accurate if $v_{sh} \gtrsim 0.2c$, at which condition we expect thermal electrons to contribute significantly to the synchrotron spectrum (Ho et al. 2021b; Margalit & Quataert 2021).

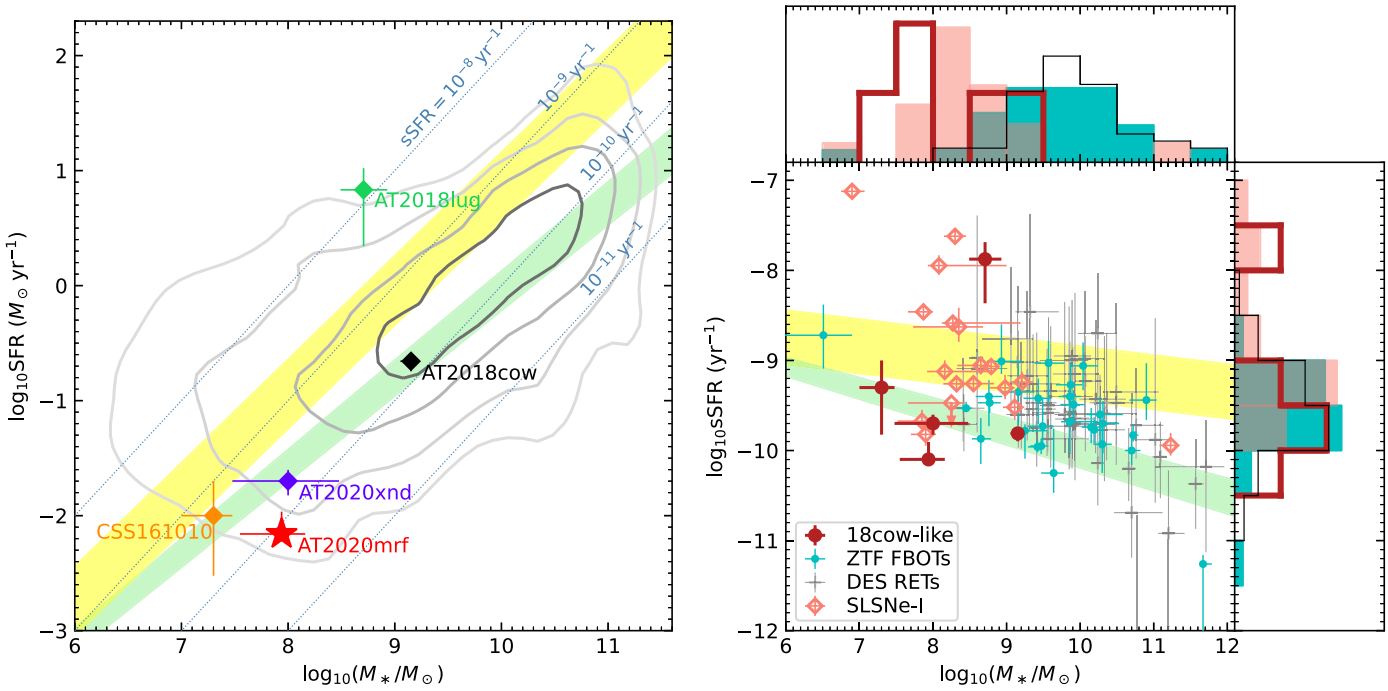

Figure 15. *Left-hand panel*: the host galaxy of AT2020mrf on the SFR–M_* diagram, compared to hosts of other AT2018cow-like events: AT2018cow itself (Perley et al. 2019), AT2018lug (Ho et al. 2020), CSS161010 (Coppejans et al. 2020), and AT2020xnd (Perley et al. 2021). For comparison, the gray contours show the PTF/iPTF CCSNe host galaxy sample (Schulze et al. 2021), from 0.5σ to 2σin steps of 0.5σ. The light green and yellow bands show the main sequence of star-forming galaxies at $0.02 < z < 0.085$ (Renzini & Peng 2015) and $z \sim 1$ (Equation (4) of Elbaz et al. 2007), respectively. *Right-hand panel*: the host galaxies of AT2018cow-like events and other massive star explosions on the sSFR–M_* diagram. Histograms show the normalized distribution of 18cow-like events (thick line, unfilled), DES RETs (thin line, unfilled), ZTF FBOTs (dark filled), and SLSNe-I (light filled).

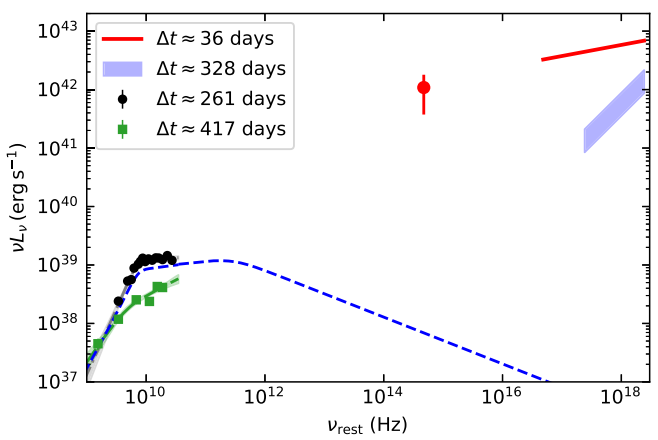

Figure 16. SED of AT2020mrf. The dashed blue line shows an example synchrotron spectrum one would expect at the epoch of the Chandra observation ($\Delta t \approx 328$ days). Here, we have assumed $B \sim 0.2$ G and a cooling frequency of $\nu_c = \gamma_c^2 \nu_g \sim 3 \times 10^{11}$ Hz, where $\gamma_c = 6\pi m_e c/(\sigma_T B^2 t)$ and $\nu_g = eB/(2\pi m_e c)$ (Sari et al. 1998; Granot & Sari 2002). Therefore, the late-time X-ray emission is much brighter than the synchrotron spectrum.

3.4.3. Stellar Mass Black Hole Engine

The engine of AT2020mrf can be a stellar mass BH, where X-rays are powered by accretion. The isotropic equivalent luminosity of 10^{42}–10^{43} erg s^{-1} corresponds to an Eddington ratio of $L_{\rm engine}/L_{\rm Edd} > 10^4$–$10^3$ for a $10\,M_\odot$ BH, which suggests that the emission is likely to be beamed.

In the case of a failed explosion, t_e is determined by the freefall of the stellar envelope (Quataert & Kasen 2012; Fernández et al. 2018):

$$t_{\rm ff} = \frac{\pi r^{3/2}}{(2GM_\star)^{1/2}} = 706\left(\frac{r}{10^{14}\ {\rm cm}}\right)^{3/2}\left(\frac{M_\star}{10\,M_\odot}\right)^{-1/2}\ {\rm day}. \quad (9)$$

To power AT2020mrf's X-ray emission out to 328 days, a weakly bound red supergiant (RSG) progenitor with $r > 6 \times 10^{13}$ cm is required. The amount of mass around the disk circularization radius is much smaller than that in the stellar envelope, and the fast X-ray variability is related to the change of angular momentum in the accreting material (Quataert et al. 2019).

In the case of a successful explosion, the accretion is supplied by fallback of bound material (Dexter & Kasen 2013). In compact progenitors such as blue supergiants (BSGs), a reverse shock decelerates the inner layers of the ejecta, resulting in enhanced fallback mass (Zhang et al. 2008). The fast X-ray variability might be caused by disk instability because the viscous time is much shorter than the fallback time. The temporal coverage of our X-ray data is poor. It is possible that L_e decays shallower than $t^{-1.3}$ initially, followed by a steeper decay (e.g., $L_e \propto t^{-5/3}$) due to fallback. This might be consistent with a range of SN energies, with lower energies corresponding to later transition times between an early and less steep light curve to a later steeper fallback light curve (Quataert & Kasen 2012).

3.4.4. Millisecond Magnetar Engine

Another speculation is that the engine of AT2020mrf is a young magnetar (i.e., an extremely magnetized neutron star), where L_e is primarily provided by rotational energy loss due to

Table 7
The Detection Rates ($\dot{N}_{\rm det}$ in $\rm yr^{-1}$) of Events Similar to AT2018cow and AT2020mrf in X-Ray Surveys, Under three Different Assumptions of the Event Volumetric Rates ($\mathcal{R}$ in $\rm Gpc^{-3}\,yr^{-1}$)

Survey	f_{-13}	$D_{\rm max}$	$\dot{N}_{\rm det}$ if $\mathcal{R}=2.1$	$\dot{N}_{\rm det}$ if $\mathcal{R}=70$	$\dot{N}_{\rm det}$ if $\mathcal{R}=420$
SRG/eROSITA	1.8	373	0.080	2.7	16
		964	1.7	57	340
Einstein Probe	20	112	0.012	0.41	2.5
		289	0.21	7.1	43

Note. $D_{\rm max}$ is given in Mpc. The values in the first and third rows assume an X-ray light-curve shape similar to AT2018cow. The values in the second and fourth rows assume a conservative light-curve shape similar to AT2020mrf, and therefore the derived $\dot{N}_{\rm det}$ should be taken as lower limits.

spindown. For a neutron star with a spin period of $P_{\rm ms}\equiv P/(1\,{\rm ms})$ and a mass of $1.4\,M_\odot$, the rotational energy is $E_{\rm rot}\approx 2.5\times10^{52}P_{\rm ms}^{-2}$ erg (Kasen & Bildsten 2010; Kasen 2017). The spin period required to power $E_{\rm e}$ is thus $P\lesssim 17$ ms. If the NS has a radius of 10 km and a magnetic field of $B_{14}\equiv B/(10^{14}\,{\rm G})$, then the characteristic spindown timescale is $t_{\rm spindown}\approx 0.5B_{14}^{-2}P_{\rm ms}^{2}$ day. The luminosity extracted from spindown is roughly constant when $t\lesssim t_{\rm spindown}$, and decays as $L_{\rm e}\propto t^{-2}$ afterwards. Extrapolating the Chandra detection back to the SRG luminosity suggests that the transition occurs at ~73 days, which implies $B\lesssim 1.4\times10^{14}$ G. This is similar to the B field required to power AT2018cow inferred by Margutti et al. (2019).

In this scenario, X-rays are generated in a "nebula" region of electron/positron pairs and radiation inflated by a relativistic wind behind the SN ejecta (Vurm & Metzger 2021). Additional energy injection by fallback accretion widens the parameter space of magnetar birth properties, and predicts a late-time light-curve decay that is shallower or steeper than $L_{\rm e}\propto t^{-2}$ (Metzger et al. 2018). The day-timescale X-ray variability can be accounted for by magnetically driven mini-outbursts.

4. The Detection Rate in X-Ray Surveys

AT2020mrf is the first multi-wavelength FBOT identified from X-ray surveys. This motivates us to estimate the rate of such events in present and future X-ray surveys. The core collapse SN rate is $R=7\times10^{4}\,{\rm Gpc^{-3}\,yr^{-1}}$ (Li et al. 2011). The birthrate of 18cow-like events estimated by ZTF is $\mathcal{R}=3\times10^{-5}$–$6\times10^{-3}R$ (Ho et al. 2021a), or 2.1–420 $\rm Gpc^{-3}\,yr^{-1}$.

Here, we assume that a multi-wavelength FBOT has an X-ray light curve that is either similar to AT2018cow itself or similar to AT2020mrf. We approximate the 0.3–10 keV X-ray luminosity of AT2018cow as a plateau with a luminosity of $L_{\rm X,p0}=3\times10^{42}\,{\rm erg\,s^{-1}}$ and a duration of $t_{\rm X,p0}=30$ days (Figure 7). The light-curve shape of AT2020mrf is less well constrained. For simplicity, we assume a conservative shape consisting of two plateaus, with $L_{\rm X,p1}=2\times10^{43}\,{\rm erg\,s^{-1}}$, $t_{\rm X,p1}=36$ days, $L_{\rm X,p2}=1\times10^{42}\,{\rm erg\,s^{-1}}$, and $t_{\rm X,p2}=350$ days.

The transient detection rate is

$$\dot{N}_{\rm det}=\frac{\Omega}{3}D_{\rm max}^{3}\,\mathcal{R}\cdot p_{\rm s} \quad (10)$$

where Ω is the solid angle of the surveyed area ($\Omega=4\pi$ for an all-sky survey), $D_{\rm max}$ is the maximum distance out to which the source can be detected, and $p_{\rm s}$ is the probability that the transient is "on" when being scanned by the X-ray survey. If the survey cadence is shorter than the transient duration, then $p_{\rm s}=1$. By setting a survey flux threshold of $f_{\rm thre}=10^{-13}f_{-13}\,{\rm erg\,cm^{-2}\,s^{-1}}$, we have $4\pi D_{\rm max}^{2}\,f_{\rm thre}=L_{\rm X,p}$.

On average, every 0.5 yr, SRG/eROSITA samples the same region of the sky over ~12 passes within ~2 days. For a single event, somewhere on the sky, with an X-ray light curve shape similar to AT2018cow, the probability of being imaged by SRG during its X-ray active phase is $p_{\rm s0}=2\times(t_{\rm X,p0}+2)/365=0.175$. For a light-curve shape similar to AT2020mrf, $p_{\rm s1}=2\times(t_{\rm X,p1}+2)/365=0.208$, and $p_{\rm s2}\sim1$. The sensitivity of an eROSITA single sky survey is $\approx2.5\times10^{-14}\,{\rm erg\,s^{-1}\,cm^{-2}}$ (see Figure 17 of Sunyaev et al. 2021). In reality, to be selected as a transient by eRASSn ($n>1$), the source needs to exceed the eRASS1 sensitivity limit by a factor of ≈7. Therefore, the flux threshold is $f_{-13}\approx1.8$.

The Einstein Probe (EP) is a lobster-eye telescope that will monitor the X-ray sky (Yuan et al. 2018) and is due to be launched at the end of 2022. With an orbital period of 97 min, the entire sky can be covered over three successive orbits. Here, we assume that its Wide-field X-ray telescope (WXT) is 2 orders of magnitude more sensitive than the Monitor of All-sky X-ray Image (MAXI) mission.[17] MAXI has a transient triggering threshold of 8 mCrab for 4 days (Negoro et al. 2016), leading us to assume $f_{-13}\approx20$ for EP.

The calculated detection rates in eROSITA and EP are summarized in Table 7. The rate of similar events in present and future millimeter transient surveys is given by Ho et al. (2021b) and Eftekhari et al. (2021).

5. Summary

We report multi-wavelength observations of AT2020mrf, the fifth member of the class of AT2018cow-like events (i.e., FBOTs with luminous multi-wavelength counterparts). Among the four 18cow-like events that have ever been detected in the X-ray (i.e., AT2018cow, CSS161010, AT2020xnd, AT2020mrf), AT2020mrf is the most luminous object, exhibiting day-timescale X-ray variability both at early (≈36 days) and late times (≈328 days), with a luminosity between 10^{42} and few $\times10^{43}\,{\rm erg\,s^{-1}}$. Previously, the only object showing evidence of a NS/BH central engine was AT2018cow (Margutti et al. 2019; Pasham et al. 2022). Here, we show that a compact object—a young millisecond magnetar or an accreting black hole—is required to be the central energy source of AT2020mrf (see Section 3.4).

AT2020mrf also provides accumulating evidence to show that AT2018cow-like events form another class of engine-driven massive star explosions, after long GRBs and SLSNe-I. Intriguingly, all three classes of events are preferentially hosted by dwarf galaxies. Given the MZR (Gallazzi et al. 2005; Berg et al. 2012; Kirby et al. 2013), low metallicity probably plays an important role in the formation of such exotic explosions by reducing the angular momentum loss of their progenitors (Kudritzki & Puls 2000). Local environment studies with integral-field unit (IFU) observations (e.g., Lyman et al. 2020) and high spatial resolution images (e.g., with the Hubble Space Telescope) can further illuminate the nature of their progenitors.

Although AT2018cow, AT2018lug, and AT2020xnd are FBOTs with $-20.5<M_{g,\rm peak}<-21.5$ and $t_{1/2}<5$ day, the

[17] From slide #32 of https://sites.astro.caltech.edu/~srk/XC/Notes/EP_20200923.pdf.

optical light curve of AT2020mrf is of lower peak luminosity ($M_{g,\rm peak} = -20$) and slower evolution timescale ($t_{1/2} = 7$ days). This should guide the search for such events in optical wide-field surveys to be more agnostic of the light-curve decay rate. Real-time identification of FBOTs and comprehensive spectroscopic follow-up observations are necessary to distinguish between different emission mechanisms: shock interaction with extended CSM, radioactivity, or wind reprocessing (Section 3.2.3). The discovery of X-ray emission in AT2020mrf also showcases how X-ray surveys such as SRG can be essential in the identification of multi-wavelength FBOTs.

Once identified, millimeter and radio follow-up observations are needed to reveal the CSM density as a function of distance to the progenitor, which contains information about the mass-loss history (Section 3.1). X-ray light curves provide diagnostics for the nature of the power source (Section 3.4), while broad-band X-ray spectroscopy can constrain the evolution of the geometry of the material closest to the central engine (Margutti et al. 2019). Given the late-time X-ray detections of AT2018cow at $\Delta t \approx 212$ days (Appendix A) and of AT2020mrf at $\Delta t \approx 328$ days (Section 2.4), future Chandra observations of these two objects may further constrain the timescales of their central engines.

We thank Patrick Slane for allocating DD time on Chandra. We thank the staff of Chandra, VLA, Keck, and GMRT that made these observations possible. We thank Jim Fuller, Mansi Kasliwal, Wenbin Lu, Tony Piro, and Eliot Quataert for helpful discussions. We thank the anonymous referee for constructive comments and suggestions. Y.Y. thanks Eric Burns for discussion about IPN, and Dmitry Svinkin for providing information about Konus-WIND.

Support for this work was provided by the National Aeronautics and Space Administration (NASA) through Chandra Award Number DD1-22133X issued by the Chandra X-ray Observatory Center, which is operated by the Smithsonian Astrophysical Observatory for and on behalf of NASA under contract NAS8-03060.

Y.Y. acknowledges support by the Heising-Simons Foundation. Nayana A.J. would like to acknowledge DST-INSPIRE Faculty Fellowship (IFA20-PH-259) for supporting this research. P.C. acknowledges support of the Department of Atomic Energy, Government of India, under the project no. 12-R&D-TFR-5.02-0700. P.M., M.G., S.S., G.K., and R.S. acknowledge the partial support of this research by grant 21-12-00343 from the Russian Science Foundation.

GMRT is run by the National Centre for Radio Astrophysics of the Tata Institute of Fundamental Research.

This work is based on observations with the eROSITA telescope onboard the SRG observatory. The SRG observatory was built by Roskosmos in the interests of the Russian Academy of Sciences represented by its Space Research Institute (IKI) in the framework of the Russian Federal Space Program, with the participation of the Deutsches Zentrum für Luft- und Raumfahrt (DLR). The SRG/eROSITA X-ray telescope was built by a consortium of German Institutes led by MPE, and supported by DLR. The SRG spacecraft was designed, built, launched, and is operated by the Lavochkin Association and its subcontractors. The science data are downlinked via the Deep Space Network Antennae in Bear Lakes, Ussurijsk, and Baykonur, funded by Roskosmos. The eROSITA data used in this work were processed using the eSASS software system developed by the German eROSITA consortium, and proprietary data reduction and analysis software developed by the Russian eROSITA Consortium.

The ZTF forced-photometry service was funded under the Heising-Simons Foundation grant #12540303 (PI: Graham). This work has made use of data from the ATLAS project, which is primarily funded to search for near earth asteroids through NASA grants NN12AR55G, 80NSSC18K0284, and 80NSSC18K1575; byproducts of the NEO search include images and catalogs from the survey area. This work was partially funded by Kepler/K2 grant J1944/80NSSC19K0112 and HST GO-15889, and STFC grants ST/T000198/1 and ST/S006109/1. The ATLAS science products have been made possible through the contributions of the University of Hawaii Institute for Astronomy, the Queens University Belfast, the Space Telescope Science Institute, the South African Astronomical Observatory, and The Millennium Institute of Astrophysics (MAS), Chile.

Facilities: CXO, XMM, PO:1.2 m, Keck:I (LRIS), VLA, GMRT.

Software: `astropy` (Astropy Collaboration et al. 2013), `CASA` (v5.6.1; McMullin et al. 2007), `CIAO` (Fruscione et al. 2006), `emcee` (Foreman-Mackey et al. 2013), `LPipe` (Perley 2019), `matplotlib` (Hunter 2007), `pandas` (McKinney 2010), `Prospector` (Johnson et al. 2021), `pyne2001` (Cordes & Lazio 2002), `python-fsps` (Foreman-Mackey et al. 2014), `scipy` (Virtanen et al. 2020).

Appendix A
XMM-Newton Late-time Detection of AT2018cow

AT2018cow was observed by XMM-Newton/EPIC on three epochs (PI Margutti) at rest-frame 29.6, 78.1, and 211.8 days since explosion. The first two epochs yielded clear X-ray detections, which have been reported by Margutti et al. (2019). Pasham et al. (2022) analyzed the 0.25–2.5 keV EPIC/MOS1

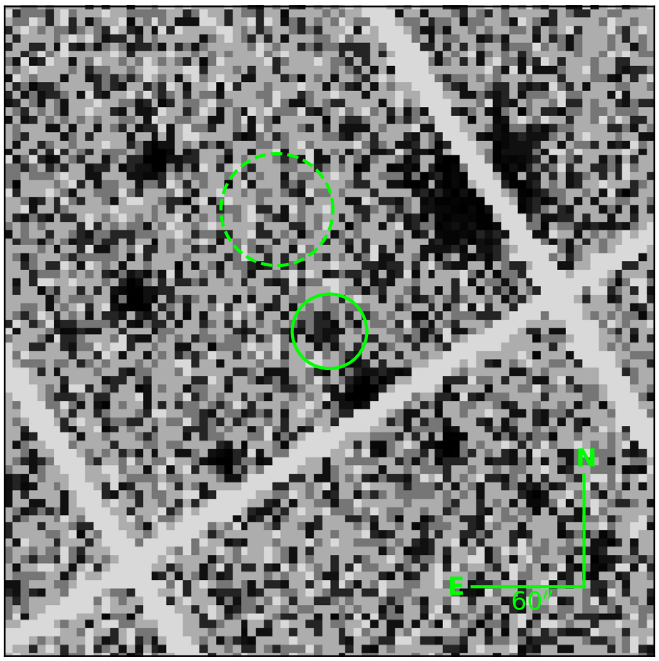

Figure 17. XMM-Newton/pn 0.3–10 keV image centered on AT2018cow, obtained at $\Delta t = 212$ days. The solid circle is the source region with $r_{\rm src} = 20''$, and the dashed circle is the background region with $r_{\rm bkg} = 30''$.

data of the third epoch, and reported a non-detection. Here, we analyze the third epoch EPIC/pn data to derive the flux (or upper limit) in 0.3–10 keV, which is important to be compared with the late-time X-ray detection of AT2020mrf. The pn instrument generally has better sensitivity than MOS1 and MOS2.

We reduced the pn data using the XMM-Newton Science Analysis System (SAS) and relevant calibration files. Events were filtered with the conditions `PATTERN <= 4` and `(FLAG&0xfb0825) == 0`. We removed high background time windows and retained 43178 s good times among the total exposure time of of 53163 s. Following Margutti et al. (2019), we extracted the source using a circular region with a radius of $r_{\rm src} = 20''$ to avoid contamination from a nearby source located $36.''8$ southwest form AT2018cow. The background is extracted from a source-free circular region with a radius of $r_{\rm bkg} = 30''$ on the same CCD (see Figure 17).

The average count rate of the source is 0.00486 count s^{-1}. The average count rate of the background (multiplied by $r_{\rm src}^2/r_{\rm bkg}^2$ to match the area of the source region) is 0.00360 count s^{-1}. Therefore, AT2018cow is detected at a (Gaussian equivalent) confidence limit of 4.2σ. Assuming an absorbed power-law model with $\Gamma \approx 2$ and $N_{\rm H} \approx 7 \times 10^{20}$ cm^{-2}, the 0.3–10 keV flux is $\sim 1.6 \times 10^{-14}$ erg s^{-1} cm^{-2}, corresponding to a luminosity of $\sim 7 \times 10^{39}$ erg s^{-1}.

Appendix B
A Sample of GRB X-Ray Light Curves

The sample of the GRB light curves shown in Figure 7 is collected as follows. We start with the list of GRBs given by the Swift GRB Table.[18] Next, we retain the 339 long GRBs ($T_{90} > 2$ s) with reported redshifts. After that, we require the last Swift/XRT detection to be at $[(t - T_0)/(1 + z)] > 20$ days, where T_0 is the GRB trigger time. This step selects 12 events, including GRB171205A ($z = 0.0368$), GRB190829A ($z = 0.078$), GRB180728A ($z = 0.12$), GRB161219B ($z = 0.15$), GRB130427A ($z = 0.34$), GRB061021 ($z = 0.35$), GRB091127 ($z = 0.49$), GRB060729 ($z = 0.54$), GRB090618 ($z = 0.54$), GRB090424 ($z = 0.54$), GRB080411 ($z = 1.0$), and GRB100814A ($z = 1.4$). We supplement the XRT light curves with deep late-time X-ray observations reported in the literature (Grupe et al. 2010; De Pasquale et al. 2017).

Appendix C
Modeling the Optical Light Curve with CSM SBO+SCE

For simplicity, we adopt the one-zone model presented in Appendix A of Margalit (2021) to fit the optical light curve of AT2020mrf. Following Yao et al. (2019), we add a constant additional variance σ_0^2 to each of the measurement variance σ_i^2 to account for systematic uncertainties. The multi-band light curves are parameterized using five free parameters: t_0, $t_{\rm dyn}$, $t_{\rm a}$, β, and E_0 (see Table 1 of Margalit 2021 for the definitions of these variables). The best-fit model is shown in Figure 18, and the posterior distribution is shown in Figure 19.

We are not able to obtain a decent fit to the observed light curves. This is due to the fact that in the CSM shock breakout and cooling model, the light-curve decay cannot be significantly slower than the rise, which makes it difficult to reproduce the "flux excess" observed at $\Delta t \sim 15$–35 days.

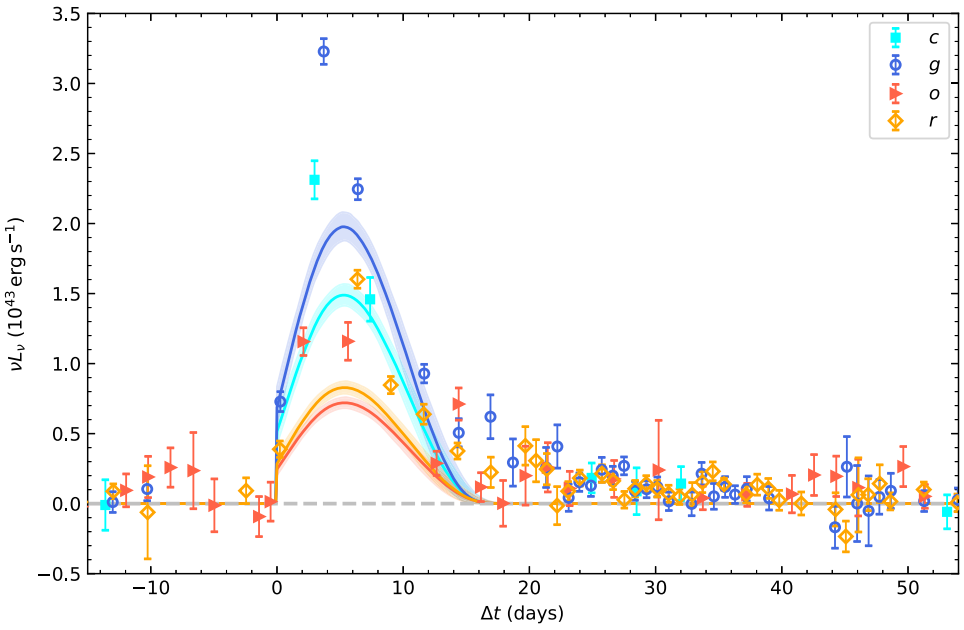

Figure 18. Dense CSM shock breakout and cooling model fit to the multi-band light curve of AT2020mrf. The maximum a posteriori model is shown via solid lines.

[18] https://swift.gsfc.nasa.gov/archive/grb_table/fullview/

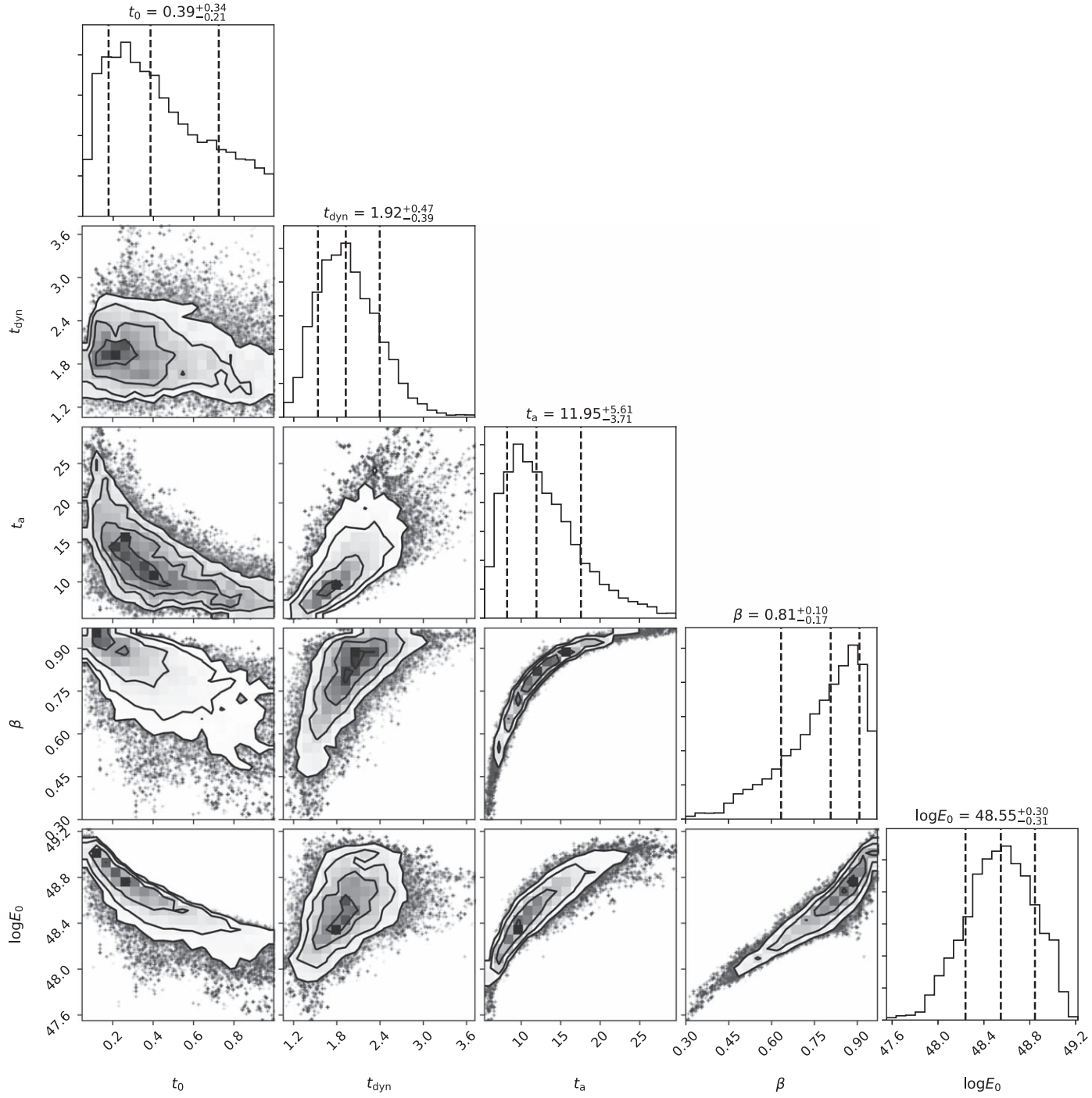

Figure 19. Corner plot showing the posterior constraints on the model parameters. Each parameter is marginalized over σ_0.

ORCID iDs

Yuhan Yao https://orcid.org/0000-0001-6747-8509
Anna Y. Q. Ho https://orcid.org/0000-0002-9017-3567
Pavel Medvedev https://orcid.org/0000-0002-9380-8708
Nayana A. J. https://orcid.org/0000-0002-8070-5400
Daniel A. Perley https://orcid.org/0000-0001-8472-1996
S. R. Kulkarni https://orcid.org/0000-0001-5390-8563
Poonam Chandra https://orcid.org/0000-0002-0844-6563
David K. Khatami https://orcid.org/0000-0003-4307-0589

References

Afsariardchi, N., Drout, M. R., Khatami, D. K., et al. 2021, ApJ, 918, 89
Aihara, H., Arimoto, N., Armstrong, R., et al. 2018, PASJ, 70, S4
Aihara, H., AlSayyad, Y., Ando, M., et al. 2019, PASJ, 71, 114
Aptekar, R. L., Frederiks, D. D., Golenetskii, S. V., et al. 1995, SSRv, 71, 265
Arnaud, K. A. 1996, in ASP Conf. Ser. 101, Astronomical Data Analysis Software and Systems V, ed. G. H. Jacoby & J. Barnes (San Francisco, CA: ASP), 17
Asplund, M., Grevesse, N., Sauval, A. J., & Scott, P. 2009, ARA&A, 47, 481
Astropy Collaboration, Robitaille, T. P., Tollerud, E. J., et al. 2013, A&A, 558, A33

Baldwin, J. A., Phillips, M. M., & Terlevich, R. 1981, PASP, 93, 5
Band, D., Matteson, J., Ford, L., et al. 1993, ApJ, 413, 281
Bellm, E. C., Kulkarni, S. R., Graham, M. J., et al. 2019, PASP, 131, 018002
Berg, D. A., Skillman, E. D., Marble, A. R., et al. 2012, ApJ, 754, 98
Bietenholz, M. F., Bartel, N., Argo, M., et al. 2021, ApJ, 908, 75
Björnsson, C.-I., & Keshavarzi, S. T. 2017, ApJ, 841, 12
Bloom, J. S., Giannios, D., Metzger, B. D., et al. 2011, Sci, 333, 203
Bright, J. S., Margutti, R., Matthews, D., et al. 2022, ApJ, 926, 112
Burke, J., Howell, D. A., Hiramatsu, D., et al. 2020, TNSCR, 2020-1846, 1
Burrows, D. N., Kennea, J. A., Ghisellini, G., et al. 2011, Natur, 476, 421
Campana, S., Mangano, V., Blustin, A. J., et al. 2006, Natur, 442, 1008
Cappellari, M. 2017, MNRAS, 466, 798
Cappellari, M., & Emsellem, E. 2004, PASP, 116, 138
Cardelli, J. A., Clayton, G. C., & Mathis, J. S. 1989, ApJ, 345, 245
Chabrier, G. 2003, PASP, 115, 763
Chandra, P., Chevalier, R. A., Chugai, N., et al. 2012, ApJ, 755, 110
Chandra, P., Chevalier, R. A., Chugai, N., Fransson, C., & Soderberg, A. M. 2015, ApJ, 810, 32
Chandra, P., Nayana, A. J., Björnsson, C. I., et al. 2019, ApJ, 877, 79
Chevalier, R. A. 1998, ApJ, 499, 810
Chevalier, R. A., & Fransson, C. 1994, ApJ, 420, 268
Condon, J. J., & Matthews, A. M. 2018, PASP, 130, 073001
Conroy, C., & Wechsler, R. H. 2009, ApJ, 696, 620
Coppejans, D. L., Margutti, R., Terreran, G., et al. 2020, ApJL, 895, L23
Cordes, J. M., & Lazio, T. J. W. 2002, arXiv:astro-ph/0207156
De Pasquale, M., Page, M. J., Kann, D. A., et al. 2017, in Proc. XII Multifrequency Behaviour of High Energy Cosmic Sources Workshop (MULTIF2017) (Trieste: PoS), 71
Dexter, J., & Kasen, D. 2013, ApJ, 772, 30
Drout, M. R., Soderberg, A. M., Gal-Yam, A., et al. 2011, ApJ, 741, 97
Drout, M. R., Chornock, R., Soderberg, A. M., et al. 2014, ApJ, 794, 23
Dwarkadas, V. V., & Gruszko, J. 2012, MNRAS, 419, 1515
Dwarkadas, V. V., Romero-Cañizales, C., Reddy, R., & Bauer, F. E. 2016, MNRAS, 462, 1101
Eftekhari, T., Berger, E., Metzger, B. D., et al. 2021, arXiv:2110.05494
Elbaz, D., Daddi, E., Le Borgne, D., et al. 2007, A&A, 468, 33
Falcón-Barroso, J., Sánchez-Blázquez, P., Vazdekis, A., et al. 2011, A&A, 532, A95
Fernández, R., Quataert, E., Kashiyama, K., & Coughlin, E. R. 2018, MNRAS, 476, 2366
Foreman-Mackey, D., Hogg, D. W., Lang, D., & Goodman, J. 2013, PASP, 125, 306
Foreman-Mackey, D., Sick, J., & Johnson, B. 2014, python-fsps: Python bindings to FSPS (v0.1.1), v0.1.1, Zenodo, doi: 10.5281/zenodo.12157
Fox, O. D., & Smith, N. 2019, MNRAS, 488, 3772
Frail, D. A., Kulkarni, S. R., Sari, R., et al. 2001, ApJL, 562, L55
Fransson, C., Lundqvist, P., & Chevalier, R. A. 1996, ApJ, 461, 993
Fruscione, A., McDowell, J. C., Allen, G. E., et al. 2006, Proc. SPIE, 6270, 62701V
Gaia Collaboration, Brown, A. G. A., Vallenari, A., et al. 2021, A&A, 649, A1
Gal-Yam, A. 2019, ARA&A, 57, 305
Gal-Yam, A., Bruch, R., Schulze, S., et al. 2022, Natur, 601, 201
Galama, T. J., Vreeswijk, P. M., van Paradijs, J., et al. 1998, Natur, 395, 670
Gallazzi, A., Charlot, S., Brinchmann, J., White, S. D. M., & Tremonti, C. A. 2005, MNRAS, 362, 41
Garmire, G. P., Bautz, M. W., Ford, P. G., Nousek, J. A., & Ricker, G. R. J. 2003, Proc. SPIE, 4851, 28
Gehrels, N. 1986, ApJ, 303, 336
Goodman, J. 1997, NewA, 2, 449
Graham, M. J., Kulkarni, S. R., Bellm, E. C., et al. 2019, PASP, 131, 078001
Granot, J., & Sari, R. 2002, ApJ, 568, 820
Grupe, D., Burrows, D. N., Wu, X.-F., et al. 2010, ApJ, 711, 1008
Gupta, Y., Ajithkumar, B., Kale, H. S., et al. 2017, CSci, 113, 707
Ho, A. Y. Q., Phinney, E. S., Ravi, V., et al. 2019, ApJ, 871, 73
Ho, A. Y. Q., Perley, D. A., Kulkarni, S. R., et al. 2020, ApJ, 895, 49
Ho, A. Y. Q., Perley, D. A., Gal-Yam, A., et al. 2021a, arXiv:2105.08811
Ho, A. Y. Q., Margalit, B., Bremer, M., et al. 2022, ApJ, 932, 116
Huang, K., Shimoda, J., Urata, Y., et al. 2019, ApJL, 878, L25
Hunter, J. D. 2007, CSE, 9, 90
Hurley, K., Golenetskii, S., Aptekar, R., et al. 2010, in AIP Conf. Ser. 1279, Deciphering the Ancient Universe with Gamma-ray Bursts, ed. N. Kawai & S. Nagataki (Melville, NY: AIP), 330
Immler, S., Modjaz, M., Landsman, W., et al. 2008, ApJL, 674, L85
Johnson, B. D., Leja, J., Conroy, C., & Speagle, J. S. 2021, ApJS, 254, 22
Kamble, A., Margutti, R., Soderberg, A. M., et al. 2016, ApJ, 818, 111
Kasen, D. 2017, in Unusual Supernovae and Alternative Power Sources, ed. A. W. Alsabti & P. Murdin (Berlin: Springer), 939
Kasen, D., & Bildsten, L. 2010, ApJ, 717, 245
Katsuda, S., Maeda, K., Bamba, A., et al. 2016, ApJ, 832, 194
Kennicutt, R. C. J. 1998, ApJ, 498, 541
Kewley, L. J., Groves, B., Kauffmann, G., & Heckman, T. 2006, MNRAS, 372, 961
Khatami, D. K., & Kasen, D. N. 2019, ApJ, 878, 56
Kirby, E. N., Cohen, J. G., Guhathakurta, P., et al. 2013, ApJ, 779, 102
Kouveliotou, C., Woosley, S. E., Patel, S. K., et al. 2004, ApJ, 608, 872
Kudritzki, R.-P., & Puls, J. 2000, ARA&A, 38, 613
Kuin, N. P. M., Wu, K., Oates, S., et al. 2019, MNRAS, 487, 2505
Lacy, M., Baum, S. A., Chandler, C. J., et al. 2020, PASP, 132, 035001
Leloudas, G., Schulze, S., Krühler, T., et al. 2015, MNRAS, 449, 917
Levan, A. J., Read, A. M., Metzger, B. D., Wheatley, P. J., & Tanvir, N. R. 2013, ApJ, 771, 136
Li, W., Chornock, R., Leaman, J., et al. 2011, MNRAS, 412, 1473
Lyman, J. D., Bersier, D., James, P. A., et al. 2016, MNRAS, 457, 328
Lyman, J. D., Galbany, L., Sánchez, S. F., et al. 2020, MNRAS, 495, 992
Madau, P., & Dickinson, M. 2014, ARA&A, 52, 415
Madsen, K. K., Beardmore, A. P., Forster, K., et al. 2017, AJ, 153, 2
Mangano, V., Burrows, D. N., Sbarufatti, B., & Cannizzo, J. K. 2016, ApJ, 817, 103
Margalit, B. 2021, arXiv:2107.04048
Margalit, B., & Quataert, E. 2021, ApJL, 923, L14
Margutti, R., Soderberg, A. M., Wieringa, M. H., et al. 2013, ApJ, 778, 18
Margutti, R., Chornock, R., Metzger, B. D., et al. 2018, ApJ, 864, 45
Margutti, R., Metzger, B. D., Chornock, R., et al. 2019, ApJ, 872, 18
Marino, R. A., Rosales-Ortega, F. F., Sánchez, S. F., et al. 2013, A&A, 559, A114
Martin, D. C., Fanson, J., Schiminovich, D., et al. 2005, ApJL, 619, L1
Masci, F. J., Laher, R. R., Rusholme, B., et al. 2019, PASP, 131, 018003
McKinney, W. 2010, in Proc. 9th Python in Science Conf., ed. S. van der Walt & J. Millman, 51
McMullin, J. P., Waters, B., Schiebel, D., Young, W., & Golap, K. 2007, in ASP Conf. Ser. 376, Astronomical Data Analysis Software and Systems XVI, ed. R. A. Shaw, F. Hill, & D. J. Bell (San Francisco, CA: ASP), 127
Metzger, B. D. 2022, ApJ, 932, 84
Metzger, B. D., Beniamini, P., & Giannios, D. 2018, ApJ, 857, 95
Meza, N., & Anderson, J. P. 2020, A&A, 641, A177
Modjaz, M., Liu, Y. Q., Bianco, F. B., & Graur, O. 2016, ApJ, 832, 108
Nayana, A. J., & Chandra, P. 2021, ApJL, 912, L9
Negoro, H., Kohama, M., Serino, M., et al. 2016, PASJ, 68, S1
Ofek, E. O., Fox, D., Cenko, S. B., et al. 2013, ApJ, 763, 42
Oke, J. B., Cohen, J. G., Carr, M., et al. 1995, PASP, 107, 375
Pasham, D. R., Ho, W. C. G., Alston, W., et al. 2022, NatAs, 6, 249
Pavlinsky, M., Tkachenko, A., Levin, V., et al. 2021, A&A, 650, A42
Perley, D. A. 2019, PASP, 131, 084503
Perley, D. A., Quimby, R. M., Yan, L., et al. 2016a, ApJ, 830, 13
Perley, D. A., Tanvir, N. R., Hjorth, J., et al. 2016b, ApJ, 817, 8
Perley, D. A., Mazzali, P. A., Yan, L., et al. 2019, MNRAS, 484, 1031
Perley, D. A., Ho, A. Y. Q., Yao, Y., et al. 2021, MNRAS, 508, 5138
Perley, D. A., Sollerman, J., Schulze, S., et al. 2022, ApJ, 927, 180
Perley, R. A., Chandler, C. J., Butler, B. J., & Wrobel, J. M. 2011, ApJL, 739, L1
Pettini, M., & Pagel, B. E. J. 2004, MNRAS, 348, L59
Piro, A. L., Haynie, A., & Yao, Y. 2021, ApJ, 909, 209
Piro, A. L., & Lu, W. 2020, ApJ, 894, 2
Predehl, P., Andritschke, R., Arefiev, V., et al. 2021, A&A, 647, A1
Prentice, S. J., Maguire, K., Smartt, S. J., et al. 2018, ApJL, 865, L3
Prentice, S. J., Ashall, C., James, P. A., et al. 2019, MNRAS, 485, 1559
Pursiainen, M., Childress, M., Smith, M., et al. 2018, MNRAS, 481, 894
Quataert, E., & Kasen, D. 2012, MNRAS, 419, L1
Quataert, E., Lecoanet, D., & Coughlin, E. R. 2019, MNRAS, 485, L83
Renzini, A., & Peng, Y.-j 2015, ApJL, 801, L29
Rivera Sandoval, L. E., Maccarone, T. J., Corsi, A., et al. 2018, MNRAS, 480, L146
Sari, R., Piran, T., & Narayan, R. 1998, ApJL, 497, L17
Sazonov, S., Gilfanov, M., Medvedev, P., et al. 2021, MNRAS, 508, 3820
Schlafly, E. F., & Finkbeiner, D. P. 2011, ApJ, 737, 103
Schrøder, S. L., MacLeod, M., Loeb, A., Vigna-Gómez, A., & Mandel, I. 2020, ApJ, 892, 13
Schulze, S., Yaron, O., Sollerman, J., et al. 2021, ApJS, 255, 29
Smith, K. W., Smartt, S. J., Young, D. R., et al. 2020, PASP, 132, 085002
Smith, N. 2017, in Interacting Supernovae: Types IIn and Ibn, ed. A. W. Alsabti & P. Murdin (Berlin: Springer), 403

Soderberg, A. M., Kulkarni, S. R., Nakar, E., et al. 2006, Natur, 442, 1014
Soker, N. 2022, RAA, 22, 055010
Soker, N., Grichener, A., & Gilkis, A. 2019, MNRAS, 484, 4972
Sonbas, E., Gronwall, C., Klingler, N. J., et al. 2020, GCN, 27915, 1
Speagle, J. S., Steinhardt, C. L., Capak, P. L., & Silverman, J. D. 2014, ApJS, 214, 15
Sunyaev, R., Arefiev, V., Babyshkin, V., et al. 2021, A&A, 656, A132
Swarup, G. 1991, in ASP Conf. Ser. 131, Radio Interferometry. Theory, Techniques, and Applications, ed. T. J. Cornwell & R. A. Perley (San Francisco, CA: ASP), 376
Taddia, F., Stritzinger, M. D., Bersten, M., et al. 2018, A&A, 609, A136
Taggart, K., & Perley, D. A. 2021, MNRAS, 503, 3931
Tiengo, A., Mereghetti, S., Ghisellini, G., Tavecchio, F., & Ghirlanda, G. 2004, A&A, 423, 861
Tonry, J., Denneau, L., Heinze, A., et al. 2020, TNSTR, 2020-1802, 1
Tonry, J. L., Denneau, L., Heinze, A. N., et al. 2018, PASP, 130, 064505
Tsvetkova, A., Frederiks, D., Svinkin, D., et al. 2021, ApJ, 908, 83
Valenti, S., Benetti, S., Cappellaro, E., et al. 2008, MNRAS, 383, 1485
Vergani, S. D., Salvaterra, R., Japelj, J., et al. 2015, A&A, 581, A102
Virtanen, P., Gommers, R., Oliphant, T. E., et al. 2020, NatMe, 17, 261
Vurm, I., & Metzger, B. D. 2021, ApJ, 917, 77
Waxman, E., & Katz, B. 2017, in Shock Breakout Theory, ed. A. W. Alsabti & P. Murdin (Berlin: Springer), 967
Whitesides, L., Lunnan, R., Kasliwal, M. M., et al. 2017, ApJ, 851, 107
Wilkes, B., & Tucker, W. 2019, The Chandra X-ray Observatory (Bristol: IOP Publishing), 2514
Willingale, R., Starling, R. L. C., Beardmore, A. P., Tanvir, N. R., & O'Brien, P. T. 2013, MNRAS, 431, 394
Wiseman, P., Pursiainen, M., Childress, M., et al. 2020, MNRAS, 498, 2575
Xiang, D., Wang, X., Lin, W., et al. 2021, ApJ, 910, 42
Yao, Y., Miller, A. A., Kulkarni, S. R., et al. 2019, ApJ, 886, 152
Yao, Y., De, K., Kasliwal, M. M., et al. 2020, ApJ, 900, 46
Yuan, W., Zhang, C., Ling, Z., et al. 2018, Proc. SPIE, 10699, 1069925
Zapartas, E., de Mink, S. E., Izzard, R. G., et al. 2017, A&A, 601, A29
Zhang, W., Woosley, S. E., & Heger, A. 2008, ApJ, 679, 639